J. Fluid Mech. (2002), *vol.* 460, *pp.* 241–280.
DOI: 10.1017/S0022112002008145 Printed in the United Kingdom

Finite-Weber-number motion of bubbles through a nearly inviscid liquid

By VOLODYMYR I. KUSHCH[1], ASHOK S. SANGANI[1], PETER D. M. SPELT[2] AND DONALD L. KOCH[3]

[1]Department of Chemical Engineering and Materials Science, Syracuse University, Syracuse, NY 13244, USA

[2]Center for Composite Materials, Imperial College, London SW7 2BY, UK

[3]School of Chemical Engineering, Cornell University, Ithaca, NY 14853, USA

(Received 14 May 2001 and in revised form 29 November 2001)

A method is described for computing the motion of bubbles through a liquid under conditions of large Reynolds and finite Weber numbers. Ellipsoidal harmonics are used to approximate the shapes of the bubbles and the flow induced by the bubbles, and a method of summing flows induced by groups of bubbles, using a fast multipole expansion technique is employed so that the computational cost increases only linearly with the number of bubbles. Several problems involving one, two and many bubbles are examined using the method. In particular, it is shown that two bubbles moving towards each other in an impurity-free, inviscid liquid touch each other in a finite time. Conditions for the bubbles to bounce in the presence of non-hydrodynamic forces and the time for bounce when these conditions are satisfied are determined. The added mass and viscous drag coefficients and aspect ratio of bubbles are determined as a function of bubble volume fraction and Weber number.

1. Introduction

Considerable work has been done in recent years to determine the equations of motion of bubbly liquids at large Reynolds and small Weber numbers (Smereka 1993; Sangani & Didwania 1993*a*, *b*; Kumaran & Koch 1993; van Wijngaarden 1993; Yurkovetsky & Brady 1996; Kang *et al.* 1997; Spelt & Sangani 1998). The Reynolds and Weber numbers are defined by $Re = 2\rho Va/\mu$ and $We = 2\rho V^2 a/\sigma$, ρ and μ being the density and viscosity of the liquid, σ the interfacial tension, a the radius of the bubbles, and V the characteristic velocity of the bubbles. In the dual limit $Re \to \infty$ and $We \to 0$ the bubbles may be approximated as spherical, and the flow induced by the motion as potential flow, thus allowing considerable simplifications in the equations of motion. Numerical simulations together with kinetic theory have made it possible to determine a complete set of equations of motion of bubbly liquids from first principles (Spelt & Sangani 1998).

Unfortunately, the dual limit is generally satisfied for a very narrow range of bubble sizes since, for a given gas–liquid system, both Re and We increase with the increase in the size and the velocity of the bubbles. It is important therefore to remove the restriction of small We before the equations of motion can be applied to practical flows of bubbly liquids. The deformation of bubbles from a spherical shape in flows at finite Weber numbers significantly affects the properties of bubbly liquids. For example, it is well known that the added mass and viscous drag coefficients of the

deformed bubbles are significantly greater than those of spherical bubbles. The shape oscillations induced by bubble–bubble interactions may also be expected to lead to a higher rate of viscous energy dissipation than for spherical bubbles.

The case of a single bubble rising with a steady velocity under the influence of buoyancy force was first examined by Moore (1965) who approximated the bubble shape to be an oblate spheroid. The aspect ratio of the spheroid as a function of Weber number was determined by satisfying the normal stress condition at only two points on the surface of the bubble. The viscous drag on the bubble and hence the rise velocity were determined using the viscous dissipation method due to Levich (1962) which makes use of the fact that the total viscous energy dissipation can be estimated to leading order (i.e. $O(Re^{-1})$) using the potential flow approximation. More rigorous analysis of the flow around a rising bubble was made Miksis, Vanden-Broeck & Keller (1981, 1982) who did not assume the shape of the bubble to be ellipsoidal. These investigators converted the potential flow problem into a nonlinear system of integro-differential equations and solved it numerically to determine the shape of the bubble more accurately by satisfying the normal stress condition on the entire surface of the bubble. These rigorous calculations showed that the approximate analysis of Moore based on a collocation method with only two points and assumed ellipsoidal shape was surprisingly accurate over a significant range of Weber numbers. Meiron (1989) also examined the problem of uniform flow past a bubble with the aim of determining the stability of the flow. He expanded the velocity potential and shape of the bubble in a series of both spherical and oblate spheroidal harmonics and used a collocation technique to determine the shape and the velocity field. He found that the series representation based on spherical surface harmonics did not converge for aspect ratio $\chi > 1.4$ while that based on ellipsoidal harmonics converged well for a wide range of aspect ratios. His results for the steady-state shape were found to be in excellent agreement with those obtained by Miksis *et al.* (1981).

The analyses mentioned above approximated the flow to be potential. Ryskin & Leal (1984) determined the flow around a single bubble by solving the Navier–Stokes equations of motion for various combinations of Weber and Reynolds numbers. Their calculations show that at large Weber numbers the bubble shape loses fore–aft symmetry, and that a region of recirculation appears on the rear side of the bubble. For example, the recirculation region is clearly seen at $Re = 200$ for $We > 4$. For such high Weber numbers the potential flow approximation is not uniformly valid. Thus, the potential flow based approximations can be expected to be reliable only for small to moderate Weber numbers. Recent progress in the study of the motion of a single bubble in rotational flows is summarized in an excellent review article by Magnaudet & Eames (2000).

Figure 1 shows the rise velocity of a bubble as a function of its equivalent spherical radius a for an air–water system. The results of Moore (1965) for non-spherical bubbles are essentially the same as those obtained by Miksis *et al.* (1981), and are shown in figure 1 by solid lines. The sensitivity of the results to the interfacial tension σ is illustrated by showing theoretical predictions of Moore for two different values of σ. The dashed line corresponds to the results for spherical bubbles. The open circles represent the experimental data for the rise velocity by Duineveld (1995). These measurements were carried out in very clean water. The solid circle represents the data recently obtained by Zenit, Koch & Sangani (2001) for bubbles in water containing some salt (magnesium sulphate). We see that the results are in reasonably good agreement with Moore's theory of ellipsoidal bubbles. The rise velocity measured by Duineveld for pure water is seen to be only slightly greater than that measured

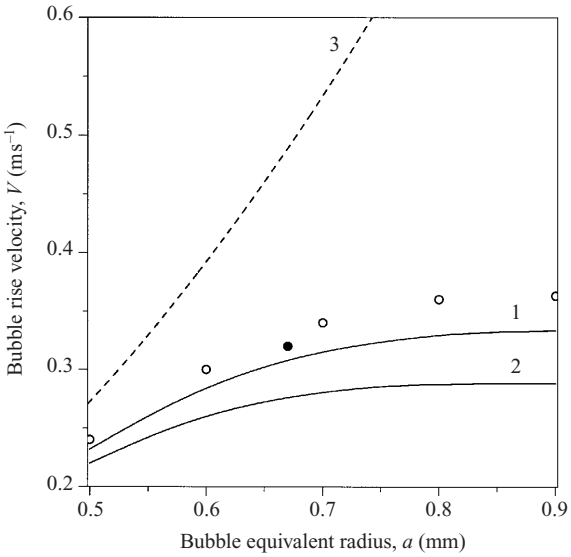

FIGURE 1. Bubble rise velocity V as a function of its radius a. The open circles show experimental data of Duineveld (1995) for 'hyper clean' water and the solid circle the value reported by Zenit *et al.* (2001) for a dilute $MgSO_4$ solution. The solid lines 1 and 2 are calculated using the Moore (1963) formula for $\sigma = 0.07$ and $\sigma = 0.05$, respectively while the dashed line 3 represents Levich's (1962) theory for a spherical bubble.

for water containing some salt. More noteworthy, however, is the observation that accounting for the deformation of bubbles leads to a significant improvement in the prediction of rise velocity and that the potential flow approximation gives reasonable estimates of the rise velocity of a bubble over a significant size range of bubbles. Thus, direct numerical simulation of the motion of interacting, deformable bubbles using a potential flow theory can be expected to improve the aforementioned analytical framework for flows of bubbly liquids based on assumption of spherical bubbles.

We describe here a method for simulating the motion of deformable bubbles. Although the flow will be approximated as potential, the method does allow for leading-order viscous effects. The method will be applied to several problems involving motion of a single bubble or interactions of two or many bubbles. In the case of a single bubble we consider both its steady motion and the motion when undergoing translation and shape oscillations. The latter case is shown to be reasonably accurately modelled by treating the bubble shape at any instant as an ellipsoid. The total kinetic energy of the liquid can be decomposed into two parts, one corresponding to the translational motion of the bubbles and the other to the shape oscillations, to be referred to as, respectively, the translational and vibrational energies. We give expressions for these two energies and the interfacial energy of a single bubble in terms of its radius and aspect ratio. It is shown that simple formulas based on treating the bubble shape at any instant as an ellipsoid for these different forms of energy give quite an accurate description of the single bubble motion. One of the motivations for carrying out single bubble calculations and interpreting them in the above manner derives from the expectation that the simplest equations of motion for bubbly liquids at finite Weber numbers will have mean bubble velocity, volume fraction and aspect ratio as primary variables, and so a kinetic theory description of

bubbly liquids will have to account for the partition of the fluctuation energy into translational, vibrational, and interfacial energies.

We next consider motion of two bubbles towards each other in an impurity-free inviscid liquid at various Weber numbers. It is shown that the distance between the two bubbles continues to decrease with time so that they will coalesce in a finite amount of time, at least for the Weber numbers less than about 3 for which the computations are carried out. This was a somewhat unexpected result since it is generally thought that the increase in the pressure in the gap between the approaching bubbles may arrest their motion at high enough Weber numbers for which the initial kinetic energy of liquid may be temporarily stored as interfacial energy before the bubbles begin to bounce (Doubliez 1991; Tsao & Koch 1994; Chesters & Hoffman 1982). Thus, the presence of impurities such as salt or surface-active impurities is necessary for the bounce to occur. Tsao & Koch (1994) have examined the case of bubbles bouncing in the presence of electrolytes. Electrolytes such as sodium chloride or magnesium sulphate are believed to induce a short-range non-hydrodyanamic repulsive force between the bubbles. These investigators considered the limit of small Weber number and showed that the time for bubbles to bounce is $O(We^{1/2})$. These investigators also reported observations on the bounce of a bubble from a wall. We calculate the bounce time as a function of Weber number. Our results for small Weber number are shown to be in agreement with the predictions of Tsao & Koch. We also compare the computed trajectory and surface area of the bubble as a function of time with those measured by Tsao & Koch for a bubble bouncing from a wall and find very good agreement between the two even though the physical situations are somewhat different: the experiment examined bounce from a wall in deionized water while our simulations considered bounce due to the presence of another bubble in the presence of a short-range repulsive potential. The good agreement may just be fortuitous or may suggest that the interaction with a horizontal wall can be modelled using a potential flow with an image bubble. We next study the interaction of a pair of bubbles rising due to buoyancy forces acting on them as a function of the initial orientation of the pair. Spherical bubbles attract each other when they are oriented at an angle greater than 55° with the vertical. Accounting for bubble deformation does not change this result significantly. Thus, the clustering seen in the simulations of Sangani & Didwania (1993*b*) is also likely to be observed for finite Weber number flows induced by rising bubbles as long as the deformation is not sufficiently pronounced to result in deviations from potential flow. It should be noted, however, that experiments of Duineveld (1994) and de Vries (2001) suggest that bubble–bubble and bubble–wall interactions can lead to shedding of vortices and significant deviations from potential flow at even smaller Weber numbers.

Finally, we consider random arrays of oriented ellipsoids as a model of bubble suspensions at finite Weber numbers and determine their added mass, viscous drag and viscous dissipation coefficients as functions of volume fraction and aspect ratio. We also determine a relation between the aspect ratio, volume fraction, and Weber number of bubbles. The results are shown to be in very good agreement with the predictions of an effective-medium theory. The theory is used to estimate the rise velocity and mean aspect ratio of bubbles as a function of bubble volume fraction for which Zenit *et al.* (2001) recently presented experimental data. The effect of bubble interactions on aspect ratio and average properties of bubble suspensions were not available previously and therefore comparison between the theory and experiments presented in Zenit *et al.* (2001) was somewhat limited. We see that significant discrepancy between the theory and experiments still persists even after

accounting for the effect of bubble interactions at finite volume fractions. We suggest that viscous dissipation due to the presence of container walls might be significant enough to cause the discrepancy.

The numerical method is described in § 2. Single bubble motion is considered in § 3 and collision of a pair of bubbles in the presence of electrolytes is considered in § 4. Results for random arrays of bubbles and comparison with the experiments are given in § 5. Finally, § 6 summarizes important results.

2. The method

At large Reynolds number the flow past low- or moderate-Weber-number bubbles can be approximated to leading order as potential, i.e. $\boldsymbol{u} = \nabla\phi$, $\boldsymbol{u}$ being the velocity at a point in the liquid and ϕ the velocity potential. The liquid will be treated as an incompressible fluid so that the potential satisfies the Laplace equation

$$\nabla^2\phi = 0. \tag{2.1}$$

The boundary conditions for ϕ, which are the usual kinematic and stress conditions at the surface of the bubbles, will be expressed in terms of a local ellipsoidal coordinate system around each bubble in view of the fact that Moore (1965) was able to obtain reasonably accurate results for a single bubble by treating it as an ellipsoid. Thus, let the surface of a representative bubble α be expressed as

$$F(\boldsymbol{x} - \boldsymbol{x}^\alpha, t) \equiv R(\eta, \varphi, t) - \bar{\xi} = 0, \tag{2.2}$$

where $\boldsymbol{x}^\alpha$ is the centre of mass of the bubble, t is the time, and $\bar{\xi}$, η and φ and are the oblate-spheroidal coordinates of a point $\boldsymbol{x}$ on the surface of the bubble. The function R will be expanded in spheroidal surface harmonics with its axis of revolution oriented along a unit vector $\boldsymbol{m}$. Denoting by $(y_1^\alpha, y_2^\alpha, y_3^\alpha)$ the local coordinates of the point $\boldsymbol{x}$ with y_1^α measured along $\boldsymbol{m}$, we have

$$y_1^\alpha = d\bar{\xi}\eta, \quad y_2^\alpha \pm \mathrm{i}y_3^\alpha = d\xi\bar{\eta}\exp(\pm\mathrm{i}\varphi), \quad \bar{\xi}^2 = \xi^2 - 1, \quad \bar{\eta}^2 = 1 - \eta^2. \tag{2.3}$$

Here, d is the radius of the disk in the focal plane defined by $\bar{\xi} = 0$, $-1 \leqslant \eta \leqslant 1$, and $0 \leqslant \varphi \leqslant 2\pi$. The local coordinates $\boldsymbol{y}^\alpha$ are related to $\boldsymbol{x}$ by

$$x_i = x_i^\alpha(t) + o_{ij}^\alpha y_j^\alpha, \tag{2.4}$$

where the direction cosines o_{ij}^α relate the orientation of the local (related to bubble α) coordinate system to the global Cartesian coordinate systems.

If the bubble is an exact oblate spheroid then R has a constant value, and the surface of the bubble is given by $R = \bar{\xi}_0$. More general shape can be expressed in terms of a series of surface harmonics:

$$R(\eta, \varphi, t) = \sum_{k=0}^{N_s} \sum_{l=-k}^{k} R_{kl}(t) Y_{kl}(\eta, \varphi), \tag{2.5}$$

where Y_{kl} are given by

$$Y_{kl}(\eta, \varphi) = P_k^l(\eta)\exp(\mathrm{i}l\varphi), \tag{2.6}$$

P_k^l being the associated Legendre polynomial of degree k and order l, and $R_{00} = \bar{\xi}_0$.

Application of the kinematic condition yields

$$\sum_{k=0}^{N_s} \sum_{l=-k}^{k} \dot{R}_{kl} Y_{kl} + (\boldsymbol{u} - \boldsymbol{V}^\alpha) \cdot \nabla F = 0, \tag{2.7}$$

where $\dot{R}_{kl}$ is the time derivative of R_{kl}, $\boldsymbol{u} = \nabla\phi$ is the liquid velocity, and $\boldsymbol{V}^\alpha = \dot{\boldsymbol{x}}^\alpha$ is the velocity of the bubble's centroid. We shall satisfy this condition in the integral sense. Multiplying the above equation by Y_{kl}^* and integrating we obtain

$$\dot{R}_{kl} = \frac{1}{\alpha_{kl}} \int_{\eta=-1}^{1} \int_{\varphi=0}^{2\pi} [(\boldsymbol{V}^\alpha - \nabla\varphi)\cdot\nabla F]\, Y_{kl}^*\, \mathrm{d}\eta\, \mathrm{d}\varphi, \tag{2.8}$$

where Y_{kl}^* is the complex conjugate of Y_{kl} and

$$\alpha_{kl} = \int_{\eta=-1}^{1} \int_{\varphi=0}^{2\pi} Y_{kl} Y_{kl}^*\, \mathrm{d}\eta\, \mathrm{d}\varphi = \frac{4\pi}{2k+1}\frac{(k+|l|)!}{(k-|l|)!}. \tag{2.9}$$

The normal-stress boundary condition for potential flow conditions can be written as

$$p_g = p + \sigma\nabla\cdot\boldsymbol{n} = -\rho\left[\frac{\partial\phi}{\partial t} + \tfrac{1}{2}\|\nabla\phi\|^2\right] + \sigma\nabla\cdot\boldsymbol{n}, \tag{2.10}$$

where σ is the interfacial tension and $\boldsymbol{n}$ is the unit outward normal at the bubble surface. The partial derivative of ϕ with time must be evaluated at constant $\boldsymbol{x}$. This can be related to the derivative at constant η and φ by using the usual chain rule of differentiation. Multiplying the stress boundary condition by Y_{kl} and rearranging we obtain, for $k \neq 0$,

$$\frac{\mathrm{d}I_{kl}}{\mathrm{d}t} = \rho \int_{\eta=-1}^{1} \int_{\varphi=0}^{2\pi} \left[-\tfrac{1}{2}\|\nabla\phi\|^2 + (\boldsymbol{V}^\alpha + \overline{\boldsymbol{V}}^\alpha)\cdot\nabla\phi + \frac{\sigma}{\rho}\nabla\cdot\boldsymbol{n}\right] Y_{kl}\, \mathrm{d}\eta\, \mathrm{d}\varphi, \tag{2.11}$$

where I_{kl} are the moments of velocity potential defined by

$$I_{kl} = \rho \int_{\eta=-1}^{1} \int_{\varphi=0}^{2\pi} \phi\, Y_{kl}(\eta,\varphi)\, \mathrm{d}\eta\, \mathrm{d}\varphi \tag{2.12}$$

and $\overline{\boldsymbol{V}}^\alpha = \dot{\boldsymbol{y}}^\alpha = (\partial\boldsymbol{y}^\alpha/\partial\bar{\xi})(\boldsymbol{u} - \boldsymbol{V}^\alpha)\cdot\nabla F$ is a velocity due to bubble deformation. Since the density of the gas is negligible compared to that of the liquid, the gas pressure p_g is essentially uniform inside the bubble. The integral of a constant times Y_{kl} over the surface ($-1 \leqslant \eta \leqslant 1$, $0 \leqslant \varphi \leqslant 2\pi$) is zero for $k \neq 0$ and therefore the gas pressure does not contribute to the above stress condition. Modifications to the above to account for viscous and non-hydrodynamic forces acting on the bubble will be described later in §§ 2.1 and 4.2.

The numerical scheme for evaluating the trajectories of bubbles through an inviscid liquid consists of solving the Laplace equation (cf. (2.1)) for the velocity potential given the shape and moments of potential, i.e. R_{kl} and I_{kl}, at time $t = 0$. Solution of this boundary value problem is described below. Once the velocity potential is determined the velocities of the bubbles are computed using

$$\boldsymbol{V}^\alpha = \frac{3}{4\pi a^3} \int_{\partial D^\alpha} (\boldsymbol{n}\cdot\boldsymbol{u})\boldsymbol{x}\, \mathrm{d}A, \tag{2.13}$$

where ∂D^α represents the surface of bubble α. Next $\dot{R}_{kl}$ and $\dot{I}_{kl}$ are evaluated using (2.8) and (2.12). (The dot above a quantity implies the derivative with respect to time.) A Runge–Kutta scheme is used to determine R_{kl} and I_{kl} at time $t = \Delta t$, Δt being the time step for trajectory integration. The above procedure is repeated to determine the shape and motion of bubbles at subsequent times.

The orientation vector $\boldsymbol{m}$ and the parameter d defining the local curvilinear coordinate system are assumed to be constant in the above derivation. Thus, the above

expressions do not involve their time derivatives. If necessary, the re-expansion of the bubble shape function F in terms of a new set of spheroidal coordinates with a different $\boldsymbol{m}$ and d may be carried out every few time steps to provide better approximation of the bubble surface and numerical efficiency of the method.

For a finite number of bubbles in an infinitely extended liquid the velocity potential is expressed by a series

$$\phi(\boldsymbol{x},t)=\sum_{\alpha=1}^{N}\sum_{n=1}^{N_s}\sum_{m=-n}^{n}A_{nm}^{\alpha}(t)F_n^m(\boldsymbol{x}-\boldsymbol{x}^{\alpha}(t),d), \tag{2.14}$$

where F_n^m are the solid singular ellipsoidal harmonics of degree n and order m (Hobson 1931), which can be written in oblate-spheroidal coordinates as

$$F_n^m(\boldsymbol{y}^{\alpha},d)=Q_n^{-m}(\mathrm{i}\bar{\xi})P_n^m(\eta)\,\mathrm{e}^{\mathrm{i}m\varphi}, \tag{2.15}$$

where $\bar{\xi}$, η and φ are related to $\boldsymbol{y}^{\alpha}\equiv\boldsymbol{x}-\boldsymbol{x}^{\alpha}$ and d by (2.3); Q_n^m are the associate Legendre polynomials of the second kind of imaginary argument. It is more convenient, however, to use instead of $Q_n^m(\mathrm{i}\bar{\xi})$ the equivalent set of real-valued functions defined as $Q_n^m(\bar{\xi})=\mathrm{i}^{n+1}Q_n^m(\mathrm{i}\bar{\xi})$; in what follows, we will use this re-definition of Q_n^m. N_s in (2.14) represents the maximum order of harmonics used in determining ϕ. The multipoles A_{nm}^{α} at time t are determined by solving (2.12) with I_{kl} and R_{kl} specified for each bubble at time t. The integral in (2.12) is evaluated by using a Guass quadrature rule for integration along the meridian η and a uniform distribution of integration nodes in φ. The total number of points used in evaluating the double integrals depended on the desired accuracy.

For determining the velocity of the bubble the integration must be carried out for its actual surface. This can be converted to integrals over η and φ using

$$\mathrm{d}A=\frac{d^2\xi_0}{h}\|\nabla F\|\mathrm{d}\eta\,\mathrm{d}\varphi,\qquad \boldsymbol{n}=\nabla F/\|\nabla F\|, \tag{2.16}$$

where $h=(\bar{\xi}^2+\eta^2)^{-1/2}$.

The impulse of the bubble is given by

$$\boldsymbol{I}^{\alpha}=-\rho\int_{\partial D^{\alpha}}\phi\,\boldsymbol{n}\,\mathrm{d}A, \tag{2.17}$$

and its time derivative by

$$\frac{\mathrm{d}\boldsymbol{I}^{\alpha}}{\mathrm{d}t}=\rho\int_{\partial D^{\alpha}}[\tfrac{1}{2}\|\boldsymbol{u}\|^2-(\boldsymbol{n}\cdot\boldsymbol{u})\boldsymbol{u}]\,\mathrm{d}A. \tag{2.18}$$

Note that the interfacial term is absent in the above expression. For very small Weber number flows the surface tension term in (2.11) may require time steps for integration to be sufficiently small. It is slightly advantageous in this case to replace the equations with $k=1$ in (2.11) by (2.18). Similarly, (2.12) with $k=1$ is replaced by (2.17).

2.1. *Viscous effects*

The leading-order viscous effect for finite Reynolds number flows can be incorporated in the analysis by either of the two methods discussed in Sangani & Didwania (1993*b*). The first method is based on calculating the gradient of viscous energy dissipation with respect to parameters that describe the motion of the surface of the bubbles, i.e. $\dot{R}_{kl}^{\alpha}$ and $\dot{\boldsymbol{x}}^{\alpha}$ for each bubble. Since the velocity correction in the boundary layers is small, the leading-order energy dissipation can be determined from the potential flow

solution as given by (see e.g. Batchelor 1967)

$$\dot{E}_{diss} = -2\mu \sum_{\alpha=1}^{N} \int_{\partial D^\alpha} n_i \frac{\partial \phi}{\partial x_j} \frac{\partial^2 \phi}{\partial x_i \partial x_j} \, \mathrm{d}A. \tag{2.19}$$

The gradient of the above dissipation function with respect to $\dot{R}^\alpha_{kl}$ and $\boldsymbol{V}^\alpha$ is difficult and computationally inefficient. We shall use instead the second method, described below.

The second method is based on the observation that the viscous force distribution depends linearly on the parameters $(\dot{\boldsymbol{x}}^\alpha, \dot{R}^\alpha_{kl})$ of the bubble surface motion. Instead of determining the velocity correction in the boundary layers and the viscous force distribution based on the full Navier–Stokes equation (Moore 1963; Kang & Leal 1988), we consider a small-amplitude oscillatory motion of the bubble around its shape and position with the same $\dot{\boldsymbol{x}}^\alpha, \dot{R}^\alpha_{kl}$. The viscous effects in this case are confined to thin Stokes layers around the surface of each bubble. The analysis of the velocity in the Stokes layer is much easier since the convective term in the Navier–Stokes equations can be neglected for small-amplitude motion. A detailed analysis similar to one performed in Sangani (1991) suggests solving the following problem for determining the viscous correction to the inviscid, Bernoulli pressure. The viscous pressure satisfies the Laplace equation in the liquid:

$$\nabla^2 p^v = 0. \tag{2.20}$$

The normal gradient of p^v at the surface of the bubbles is related to the surface divergence of the tangential component of the traction induced by the potential flow:

$$\boldsymbol{n} \cdot \nabla p^v = \nabla_s \cdot \boldsymbol{T}_s \quad \text{on} \quad \partial D^\alpha \tag{2.21}$$

where the surface divergence operator is defined as

$$\nabla_s \cdot \boldsymbol{T}_s = \nabla \cdot \boldsymbol{T}_s - \boldsymbol{n} \cdot (\nabla \boldsymbol{T}_s \cdot \boldsymbol{n}) \tag{2.22}$$

and the tangent traction vector by

$$\boldsymbol{T}_s = \boldsymbol{T} - \boldsymbol{n}(\boldsymbol{T} \cdot \boldsymbol{n}), \quad \boldsymbol{T} = 2\mu \nabla\nabla\phi \cdot \boldsymbol{n}. \tag{2.23}$$

The boundary condition (2.21) can be expressed in the integral form

$$\int_{\partial D^\alpha} \boldsymbol{n} \cdot \nabla p^v Y^*_{kl} \, \mathrm{d}A = \int_{\partial D^\alpha} (\nabla_s \cdot \boldsymbol{T}_s) Y^*_{kl} \, \mathrm{d}A. \tag{2.24}$$

The integral on the right-hand side requires evaluating third-order partial derivatives of ϕ. An integration by parts can be used to lower the order of derivative required. For this purpose it is useful first to write the above expression in terms of contravariant surface components of vector $\boldsymbol{T}_s$ (Aris 1962). Let u^α, $\alpha = 1, 2$, be the surface coordinates of a point on the surface whose coordinates in the three-dimensional space are y_i. The contravariant surface components of $\boldsymbol{T}_s$ are defined by

$$T^\alpha_s = c^{\alpha\beta} t^i_\beta (\boldsymbol{T}_s \cdot \boldsymbol{e}_i), \quad t^i_\beta = \frac{\partial y_i}{\partial u^\beta}, \tag{2.25}$$

where the summation over i from 1 to 3 and β from 1 to 2 is implied as in the usual Einstein notation, $\boldsymbol{e}_i$ are the unit vectors in the three-dimensional space, and

$$c^{\alpha\beta} = \sum_{i=1}^{3} h_i^2 t^i_\alpha t^i_\beta, \tag{2.26}$$

h_i being the metric coefficients. For the ellipsoidal coordinate system, $u^1 = \eta$, $u^2 = \varphi$, $h_1 = h\xi/d$, $h_2 = h\bar{\eta}/d$, $h_3 = 1/(d\xi\bar{\eta})$ and $h = (\bar{\xi}^2 + \eta^2)^{-1/2}$. The surface divergence of $\boldsymbol{T}_s$ can be expressed in terms of surface contravariant components as

$$\nabla_s \cdot \boldsymbol{T}_s = \frac{1}{\sqrt{c}} \frac{\partial}{\partial u^\alpha}(\sqrt{c} T_s^\alpha), \quad c = \det \| c^{\alpha\beta} \|. \tag{2.27}$$

Substituting the above equation in (2.24) and carrying out integration by parts we obtain

$$\int (\nabla_s \cdot \boldsymbol{T}_s) Y_{kl}^* \, \mathrm{d}A = \int T_s^\beta \frac{\partial}{\partial u^\beta} Y_{kl}^* \, \mathrm{d}A \tag{2.28}$$

which requires only second-order derivatives of ϕ.

Once the viscous pressure is determined the normal stress balance (2.10) is modified by adding $p^v - 2\mu \boldsymbol{nn} : \nabla\nabla\phi$ to the right-hand side of (2.10). The integral condition (2.11) is similarly modified. The above expression can be shown to reduce to that used by Sangani & Didwania (1993*b*) for spherical bubbles. These investigators also showed that the results obtained by this method are equivalent to those obtained by the dissipation method for a pair of spherical bubbles.

Further details to treat the case of many bubbles with periodic boundary conditions are given in § 5.

3. Single bubble motion

3.1. *Steady motion*

We begin with the results for a single bubble. As mentioned in the introduction, several investigators have reported results for a uniform flow past a single bubble. Moore (1965) determined the added mass, viscous drag and aspect ratio as functions of Weber number assuming that the bubble is an oblate spheroid. We shall derive his results here briefly in terms of the ellipsoidal harmonics introduced in the previous section and then compare them with the results of numerical simulations which do not assume the shape to be spheroidal. We shall also compare the results with those by Meiron (1989) who determined the aspect ratio as a function of Weber number by a method that is different from the one outlined here.

The velocity potential for a single oblate spheroid moving steadily with velocity $\boldsymbol{V} = V\boldsymbol{e}_1$ along the x_1-axis is given by

$$\phi(\boldsymbol{x}) = A_{10} F_1^0(\boldsymbol{x}, d) = A_{10} Q_1(\bar{\xi})\eta, \quad Q_n(\bar{\xi}) = Q_n^0(\bar{\xi}). \tag{3.1}$$

The kinematic condition at steady state reduces to $\boldsymbol{n} \cdot \nabla\phi = \boldsymbol{n} \cdot \boldsymbol{V}$ at $\xi = \xi_0$. Noting that the unit normal vector $\boldsymbol{n}$ on the surface of an oblate spheroid equals the unit vector along the ξ-axis, it is easy to show that

$$A_{10} = dV/Q_1'(\bar{\xi}_0), \tag{3.2}$$

where a prime denotes differentiation of the function by its argument.

The added mass coefficient C_a for the bubble is calculated by first evaluating the impulse $\boldsymbol{I} = I_1\boldsymbol{e}_1$ with

$$I_1 = (m/2)C_a V = -\rho \int \phi n_1 \, \mathrm{d}A, \quad m = 4\pi\rho a^3/3, \tag{3.3}$$

a being the equivalent radius of a sphere having the same volume as that of the spheroid and $\boldsymbol{m}$ the mass of the liquid displaced by the spheroid. The definition of C_a

involves a factor of one-half so as to make C_a equal to unity for a spherical bubble. Using $n_1\,\mathrm{d}A = 2\pi\,\mathrm{d}^2\xi_0^2\eta\,\mathrm{d}\eta$, and integrating from $\eta = -1$ to $\eta = 1$, we obtain

$$C_a = -\frac{2Q_1(\bar{\xi}_0)}{\bar{\xi}_0 Q_1'(\bar{\xi}_0)}. \tag{3.4}$$

The following relations are useful for evaluating the added mass coefficient as a function of the aspect ratio χ of the oblate spheroid:

$$Q_1(\bar{\xi}) = 1-\bar{\xi}\tan^{-1}(1/\bar{\xi}), \quad Q_1(\bar{\xi})-\bar{\xi}Q_1'(\bar{\xi}) = 1/\xi^2, \quad (a/d)^3 = \xi_0^2\bar{\xi}_0, \quad \chi = \xi_0/\bar{\xi}_0. \tag{3.5}$$

With use of (3.5), (3.4) can be written alternatively as $C_a = -2d^2A_{10}/V - 2$. The viscous drag coefficient C_d can be determined from the viscous energy dissipation rate by means of

$$\dot{E}_{diss} = 12\pi\mu a V^2 C_d = -2\mu\int[\nabla\nabla\phi : \nabla\phi\boldsymbol{n}]\,\mathrm{d}A. \tag{3.6}$$

Substituting for the velocity potential ϕ in the above equation and evaluating the integral yields

$$C_d = \frac{1}{3(\xi_0^2\bar{\xi}_0)^{4/3}}\frac{[1-(1-\bar{\xi}_0^2)Q_1(\bar{\xi}_0)]}{[\bar{\xi}_0 Q_1'(\bar{\xi}_0)]^2}. \tag{3.7}$$

This result is just a different form of Moore's well-known formula for a viscous drag and it agrees with the drag force determined by the second method described in the previous subsection, i.e. that based on determining viscous pressure based on an equivalent bubble oscillation problem.

The above results for a single oblate spheroid are exact. To relate these results to those for a bubble moving with velocity $\boldsymbol{V}$, Moore (1965) estimated the aspect ratio by satisfying the dynamic boundary condition

$$p_g = \rho(\boldsymbol{V} - \tfrac{1}{2}\boldsymbol{u})\cdot\boldsymbol{u} + \sigma\nabla\cdot\boldsymbol{n} \tag{3.8}$$

at $\eta = 0$ and $\eta = 1$. The two unknowns χ and p_g can be determined from the two equations generated from (3.8). In particular, the aspect ratio is determined by requiring that the right-hand side of (3.8) be the same for $\eta = 0$ and 1. Let $H(\eta)$ be given by

$$H(\eta) = -\tfrac{1}{2}\|\nabla\phi - \boldsymbol{V}\|^2 + \frac{\sigma}{\rho}\nabla\cdot\boldsymbol{n}. \tag{3.9}$$

The aspect ratio is then determined by solving

$$H(0) = H(1). \tag{3.10}$$

The sum of curvatures at a point on the surface of an oblate spheroid can be evaluated from

$$\nabla\cdot\boldsymbol{n} = \frac{h^2}{d}\frac{\partial}{\partial\bar{\xi}}\left(\frac{\xi}{h}\right), \quad \nabla\cdot\boldsymbol{n}|_{\eta=0} = (1+\chi^2)\chi^{-1/3}, \quad \nabla\cdot\boldsymbol{n}|_{\eta=1} = 2\chi^{-4/3}. \tag{3.11}$$

Equation (3.10) is most conveniently solved by choosing the value of ξ, and hence the aspect ratio, and determining the Weber number from (3.9)–(3.11). The resulting aspect ratio (Moore's solution) is shown as a function of Weber number in figure 2 as a dashed line. The solid curve corresponds to the results of the more exact analysis by Meiron (1989) and reproduced by the numerical method described in § 2. Both the $\chi(We)$ curves have a turning point at $We = We_c$: Moore's analysis gives $We_c \simeq 3.74$ while Meiron's analysis gives $W_{ec} \simeq 3.35$.

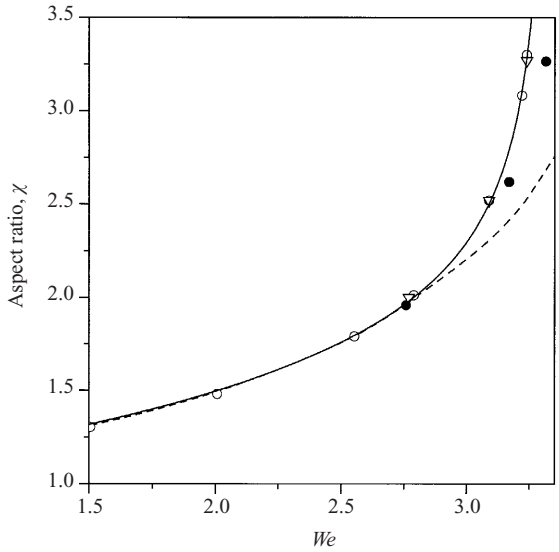

FIGURE 2. Aspect ratio χ of a bubble as a function of Weber number We. The dashed line corresponds to Moore's (1963) theory, the triangles show Meiron's (1989) numerical solution (data are taken from the plot). The results obtained by the present method are shown by the solid ($Re = 200$) and open ($Re = 400$) circles; solid line represents the fitting formula (3.12).

Meiron determined the steady state shape directly from the kinematic and nonlinear dynamic boundary conditions by using a Newton's iterative scheme. The velocity potential was expressed in terms of ellipsoidal harmonics as in the present study and the boundary conditions were satisfied at a selected number of points. In the present analysis, we solved the unsteady flow equations. The bubble was given a body force to counterbalance the viscous force at steady state. It was found that the numerical results converged with increasing N_s, the highest order multipoles retained in the calculations, and that in most cases $N_s = 6$ provided adequate accuracy. The time integration was carried out using a fourth-order Runge–Kutta scheme and a time step of 0.01 (non-dimensionalized by a/V) gave sufficiently high accuracy. The results for two Reynolds numbers $Re = 200$ and $Re = 400$ are shown in figure 2 by the solid and open circles, respectively. Further increase in Re did not change the results significantly. We see that our results for $Re = 400$ are in excellent agreement with the results of Meiron corresponding to $Re = \infty$.

The expression given by Moore (1965) is not convenient for determining the aspect ratio of a bubble given its Weber number since it explicitly gives Weber number as a function of aspect ratio. The following expression obtained by curve fitting the exact results of Meiron and the present analysis can be used in its place for estimating aspect ratio for $We \leqslant 3.3$:

$$\chi = 1 + \frac{9}{64}We + \frac{0.06We^2}{(3.37 - We)^{1/2}}. \tag{3.12}$$

Figure 3 compares the results of our numerical simulations for the added mass and viscous drag coefficients as a function of aspect ratio (and hence the Weber number for $We < We_c$) with those given by Moore (cf. (3.5) and (3.7)). Once again, the following expressions obtained by curve fitting our numerical results may be used

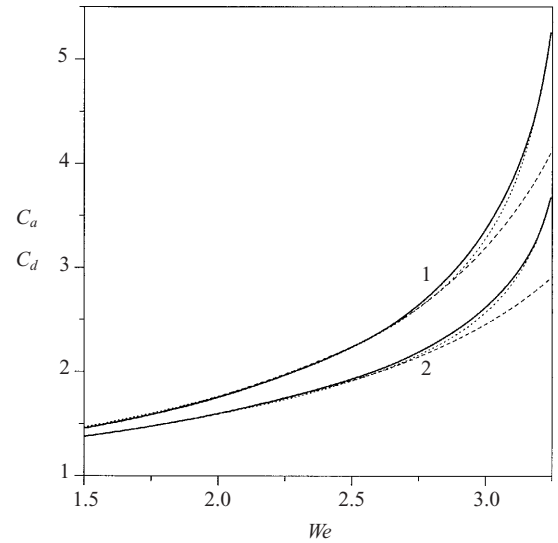

FIGURE 3. Added mass coefficient C_a (line 1) and viscous drag coefficient, C_d (2) as a function of a bubble aspect ratio obtained numerically (solid lines), from Moore's approximate solution (dashed lines), and by fitting the accurate solution by (3.13) and (3.14) (dotted lines).

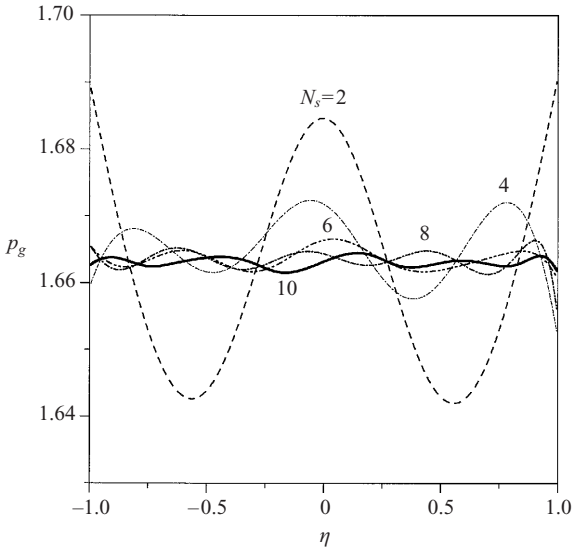

FIGURE 4. Convergence check of solution given by series (2.14), with N_s increased, by verifying the boundary condition $p_g = \text{const}$ at the bubble surface.

for evaluating the added mass and viscous drag coefficients:

$$C_a = 1 + \frac{27}{160}We + 0.072\frac{We^2}{(3.37 - We)^{1/2}}, \tag{3.13}$$

$$C_d = 1 + \frac{3}{16}We + 0.1124\frac{We^2}{(3.37 - We)^{1/2}}. \tag{3.14}$$

The dynamic boundary condition on the surface of a bubble is satisfied in our

method in the integral sense. To see how well that condition is satisfied we show in figure 4 the gas pressure p_g at the gas–liquid interface evaluated using

$$p_g = -\rho\left(\frac{\partial\phi}{\partial t} + \frac{1}{2}u^2\right) + \sigma\nabla\cdot\boldsymbol{n}. \tag{3.15}$$

In these calculations we set the viscous and buoyancy forces to zero and chose the initial aspect ratio of the bubble to be given by Moore's expression with $We = 2$. Since the initial shape did not correspond to the exact result, the bubble underwent slight shape oscillations as a function of time. The partial derivative of ϕ with time was evaluated using a backward difference approximation after a time of about one unit (non-dimensionalized by a/V). Since the density of the gas is assumed to be vanishingly small, we expect p_g to be constant. The results shown in figure 4 suggest that variation in p_g along the interface is indeed very small even with $N_s = 4$ for which the pressure variation is less than 1%. (Note that the pressure scale in the figure is considerably expanded to show the detailed variation.)

3.2. *Shape oscillations*

We next consider shape oscillations of bubbles. As mentioned in the introduction, kinetic theory for finite Weber number flows of bubble suspensions must consider both translational and vibrational (shape) oscillation modes of bubbles. We shall first derive an approximate expression for accounting for shape oscillations and then compare it with the results of numerical simulations.

The aspect ratio variations are governed primarily by the P_2-part of the velocity potential. Let

$$\phi = F_2^0(\boldsymbol{x}, d) = Q_2(\bar{\xi})P_2(\eta) \tag{3.16}$$

be the velocity potential around a spheroid of aspect ratio χ. Assuming its volume to be constant, the rate of change of aspect ratio can be determined from the normal gradient of ϕ at $\eta = 1$. This yields

$$\dot{\chi} = -\frac{3}{2}\frac{\xi_0}{d^2\bar{\xi}_0^2 Q_2'(\bar{\xi}_0)}. \tag{3.17}$$

Next, we determine the total kinetic energy of the fluid corresponding to the velocity potential (3.16) and express the result in the form

$$E_v = (m/2)C_v(a\dot{\chi})^2, \tag{3.18}$$

where E_v is the total vibrational energy, i.e. total kinetic energy resulting from a spheroid whose aspect ratio is varying with time, and C_v the vibration coefficient given by

$$C_v = -\frac{4}{15}\left(\frac{d}{a}\right)^5 \bar{\xi}^4\frac{Q_2(\bar{\xi}_0)}{Q_2'(\bar{\xi}_0)}. \tag{3.19}$$

The explicit expressions for Q_2 and Q_2' are

$$Q_2(\bar{\xi}) = \tfrac{1}{2}[-3\bar{\xi} + (1 + 3\bar{\xi}^2)\tan^{-1}(1/\bar{\xi})], \quad Q_2'(\bar{\xi}) = -3 + 1/\xi^2 + 3\bar{\xi}\tan^{-1}(1/\bar{\xi}). \tag{3.20}$$

For a spherical bubble this yields $C_v(1) = 4/45$. Now in the absence of viscous effects the sum of interfacial, translational, and vibrational energy of the fluid remains constant and therefore the motion of a single bubble undergoing translation and shape oscillations will approximately satisfy

$$E_t = (m/2)[C_a V^2 + C_v(a\dot{\chi})^2] + E_s = \text{const}, \tag{3.21}$$

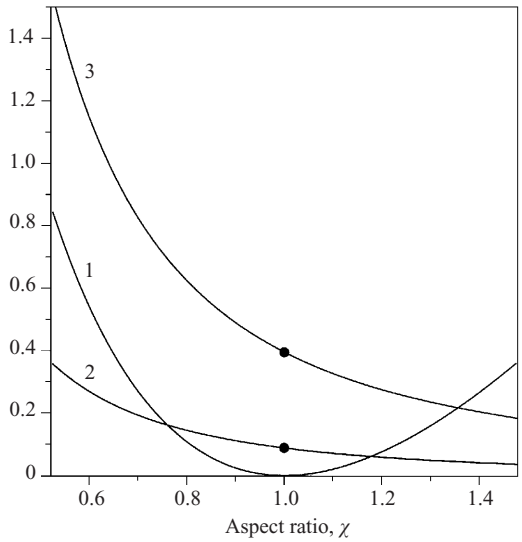

FIGURE 5. The excess surface area $S/a^2 - 4\pi$ (line 1), vibration coefficient C_v (line 2) and vibration dissipation coefficient C_{dv} (line 3) as functions of spheroidal bubble aspect ratio χ. The solid circles represent the values $C_v = 4/45$ and $C_{dv} = 32/81$ for a spherical ($\chi = 1$) bubble.

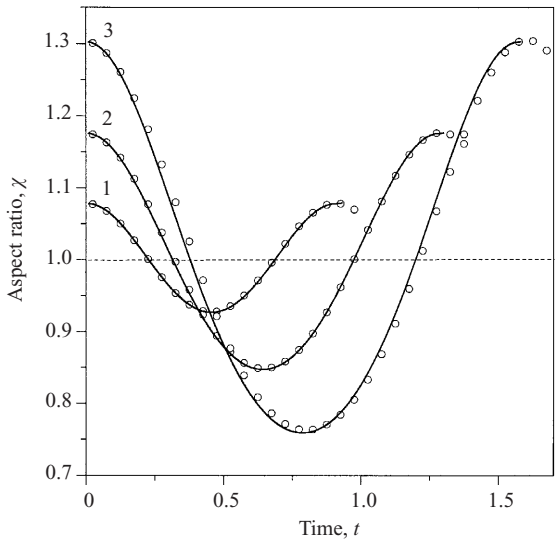

FIGURE 6. Aspect ratio χ of a freely oscillating bubble ($V = 0$) as a function of time obtained by numerical simulation (open circles) and by integrating (3.21) (solid curves). The lines 1, 2 and 3 correspond, respectively, to $We = 0.25$, 1.0 and 1.5.

where E_t is the total energy, $E_s = \sigma(S(\chi) - 4\pi a^2)$ is the excess surface energy, and S is the surface area of a spheroid with aspect ratio χ:

$$S(\chi) = 2\pi d^2 \xi_0 [\xi_0 + \bar{\xi}_0^2 Q_0(\xi_0)]. \tag{3.22}$$

Figure 5 shows C_v and $S/a^2 - 4\pi$ as functions of χ. The above expressions are approximate since the bubble shape does not correspond exactly to an ellipsoid and

since the bubble motion will induce other (P_n, $n \geqslant 3$) shape oscillation modes in addition to the P_1 and P_2 modes considered in determining the expression for the total kinetic energy of the liquid.

Figure 6 shows the aspect ratio of a bubble as a function of time. The initial shape of the bubble corresponded to Moore's solution for a steadily translating bubble with velocity V and Weber number We. To study the free oscillations of the bubble, we set $V = 0$ for $t > 0$. Since the initial ellipsoidal shape of the bubble has a surface area that is greater than the spherical bubble having the same volume, the bubble will undergo shape oscillations such that the sum of vibrational and interfacial energy will remain constant. The solid lines in figure 6 correspond to χ as a function of time obtained by integrating (3.21) which gives

$$\dot{\chi} = \pm \left(\frac{E_t - E_s}{C_v (m/2) a^2} \right)^{1/2}. \tag{3.23}$$

Initially χ decreases as the interfacial energy is converted into vibrational energy and therefore the negative sign must be used while integrating (3.23). The sign is switched subsequently every time $\dot{\chi}$ becomes zero.

The circles in figure 6 represents the results of numerical simulations with $N_s = 10$. We see that the results are in excellent agreement with the approximate theory. Small amplitude P_2-mode oscillations of spherical bubbles have a natural frequency given by

$$\omega = \left(\frac{12\sigma}{\rho a^3} \right)^{1/2}. \tag{3.24}$$

The period for one cycle computed using $2\pi/\omega$ agrees well with the results of numerical simulations, suggesting that (3.24) gives reasonably accurate estimates of the frequency of shape oscillations.

Next we consider a case where the translational velocity is non-zero. For this case we once again start with an initial shape corresponding to Moore's solution with velocity V and Weber number We. At $t = 0$ we reduce the velocity to $V/2$ to induce shape oscillations. Figure 7 shows results for aspect ratio as a function of time for three initial Weber numbers. The solid line represents the predictions of the approximate theory while the dashed lines the results of numerical simulations. The approximate theory predicts oscillatory motion while the numerical results show that the aspect ratio variation is not exactly cyclical. The coupling between the translational and vibrational mode leads to more complicated behaviour of aspect ratio as a function of time than can be predicted from the simple model given by (3.21)–(3.22). At any rate, we see that the approximate theory does give reasonably accurate predictions of the magnitude of the aspect ratio fluctuations. Figure 8 shows the translational velocity of the bubble as a function of time. Once again we see good agreement between the results of exact computations and an approximate theory based on an ellipsoidal bubble.

The amplitude of the oscillations in aspect ratio and translational velocity of the bubble will decrease with time when the fluid viscosity is finite. The energy dissipation due to motion induced by aspect ratio variations can once again be estimated by treating the bubble as an ellipsoid and considering only the P_2-mode oscillations. This yields the energy dissipation due to vibration mode be given by

$$\dot{E}_{dv} = 12\pi\mu a^3 \dot{\chi}^2 C_{dv} \tag{3.25}$$

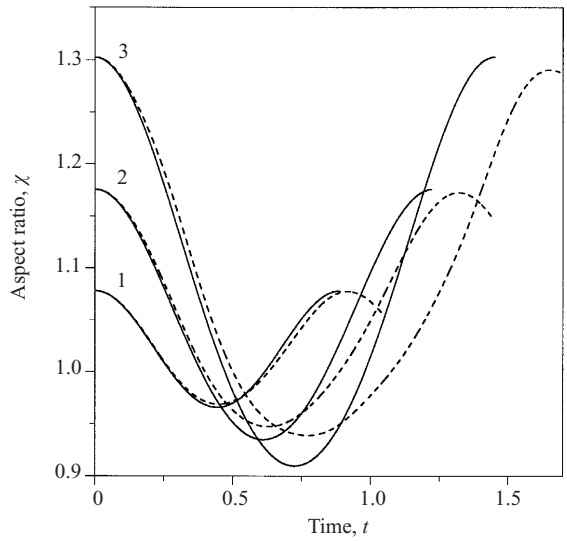

FIGURE 7. Bubble aspect ratio χ as a function of time in the case of non-zero translational velocity obtained by numerical simulation (dashed curves) and by integrating (3.21) (solid curves). The lines 1, 2 and 3 are calculated for, respectively, $We = 0.25$, 1.0 and 1.5.

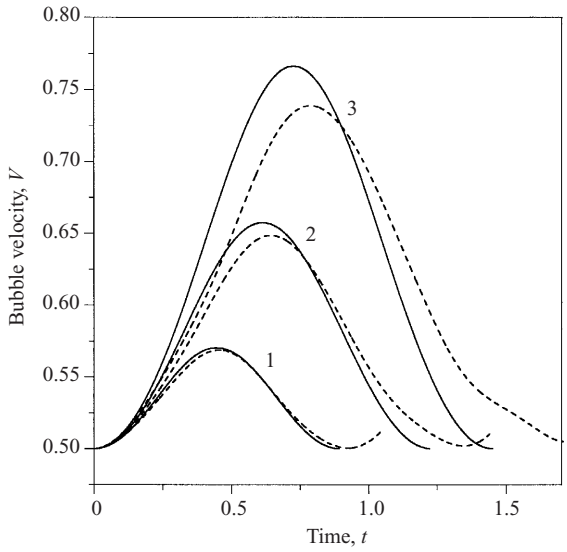

FIGURE 8. Translational velocity of an oscillating bubble as a function of time. For details of the curves, see figure 7.

with the vibration dissipation coefficient given by

$$C_{dv}(\chi) = \frac{4d^3}{27a^3}\bar{\xi}_0^3\left[1 + \frac{2Q_2(\bar{\xi}_0)}{\bar{\xi}_0\xi_0^4(Q_2'(\bar{\xi}_0))^2}\right]. \tag{3.26}$$

For a spherical bubble ($d \to 0$), the above expression yields $C_{dv}(1) = 32/81$, in agreement with a small-amplitude analysis for spherical bubbles. C_{dv} as a function of χ is given in figure 5 by line 3. Note also the simple and accurate fitting formulas $C_v(\chi) = C_v(1)\chi^{-2.158}$ and $C_{dv}(\chi) = C_{dv}(1)\chi^{-2.082}$.

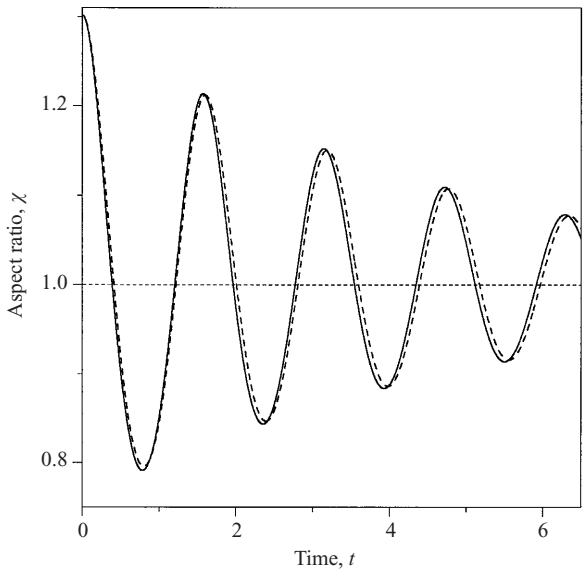

FIGURE 9. Aspect ratio χ of a freely oscillating bubble ($Re = 200$). The solid line represents solution of (3.27)–(3.28) and the dashed line the numerical solution.

The single bubble motion can be modified now to account for finite viscosity using

$$\frac{\mathrm{d}\boldsymbol{I}}{\mathrm{d}t} = -12\pi\mu a C_d \boldsymbol{V} = -12\pi\mu a (C_d/C_a)(2\boldsymbol{I}/m), \tag{3.27}$$

$$\frac{\mathrm{d}E_t}{\mathrm{d}t} = -12\pi\mu a [C_d V^2 + C_{dv}(a\dot{\chi})^2], \tag{3.28}$$

with E_t given by (3.21).

Figures 9 and 10 show comparisons between the numerical results and the predictions based on the above equations. The viscous damping of a freely oscillating bubble (with no net momentum of liquid) shown in figure 9 is very accurately predicted by (3.28). The case of a translating and oscillating bubble shown in figure 10 is predicted with lesser accuracy presumably because the model equations do not account for P_1-P_2 mode coupling. It is interesting to note that the impulse of the bubble decreases nearly steadily with time even though both the velocity and the aspect ratio show considerable oscillations.

4. Pair of bubbles

4.1. *Impurity-free liquids*

We next consider the motion of two interacting bubbles. First, we show that bubbles moving towards each other with equal and opposite velocities along their line of centres will coalesce under potential flow conditions in the absence of surface-active impurities or electrolytes.

Calculations were done for bubbles with initial relative velocity of $2V$ and separated initially by 10 bubble radii. The initial shape was assumed to be an oblate spheroid with an aspect as determined from Moore's solution. Figure 11 shows the shape of the bubbles as a function of Weber number ($We = 2a\rho V^2/\sigma$) just prior to touching. The bubbles become considerably flattened as they approach each other but fail to

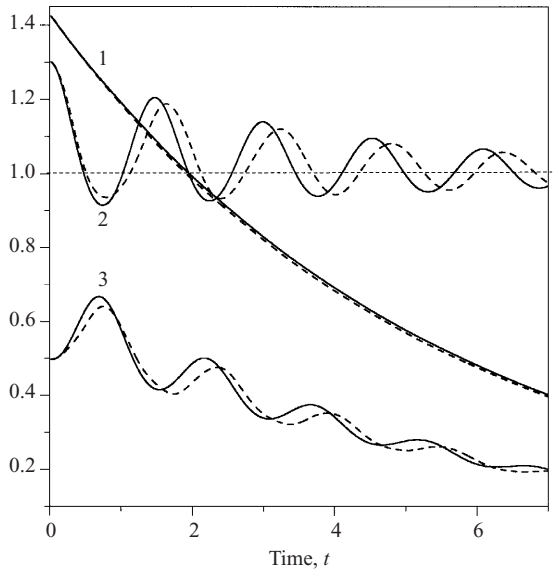

FIGURE 10. Viscous damping of impulse (line 1), aspect ratio (line 2) and translational velocity (line 3) of an oscillating bubble; $Re = 200$, $We = 1.5$. The dashed lines are obtained by numerical integration and the solid lines using the simplified model (3.27)–(3.28).

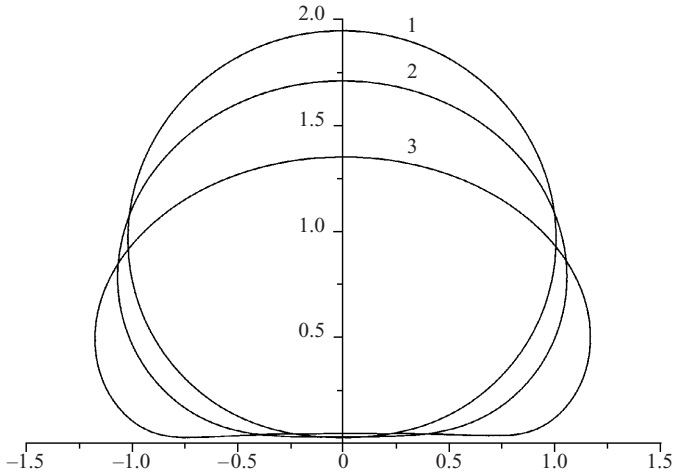

FIGURE 11. Bubble's shape just prior to touching during the approach of two equal-sized bubbles towards each other (minimum distance between the surfaces $h_{min} = 0.02a$). The contours 1, 2, and 3 correspond to initial We numbers of 0.25, 1.0 and 2.0, respectively.

convert the kinetic energy of the fluid completely into interfacial energy to arrest their motion. The calculations were carried out up to We of approximately 3, slightly less than the single-bubble critical Weber number. The viscosity of the fluid was taken to be zero. Figures 12 and 13 show the magnitude of impulse and velocity of the bubbles at the time when they come in contact. The hydrodynamic interactions between the bubbles cause an attractive force and this increases the magnitude of the impulse of the bubbles as they move towards each other. On the other hand, the relative velocity of the bubbles decreases as they approach each other in spite

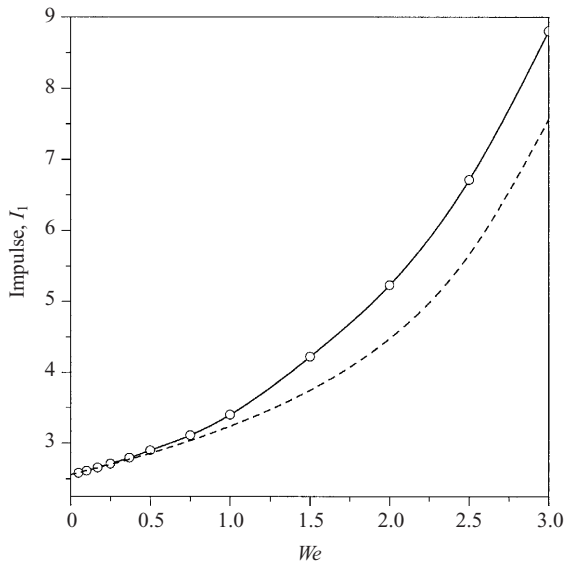

FIGURE 12. The magnitude of bubble impulse I_1 just prior to touching the other bubble as a function of initial Weber number for a bubble of a general shape given by (2.5) (solid line) and a spheroidal bubble with variable aspect ratio ($N_s = 2$ in (2.5)) (dashed line).

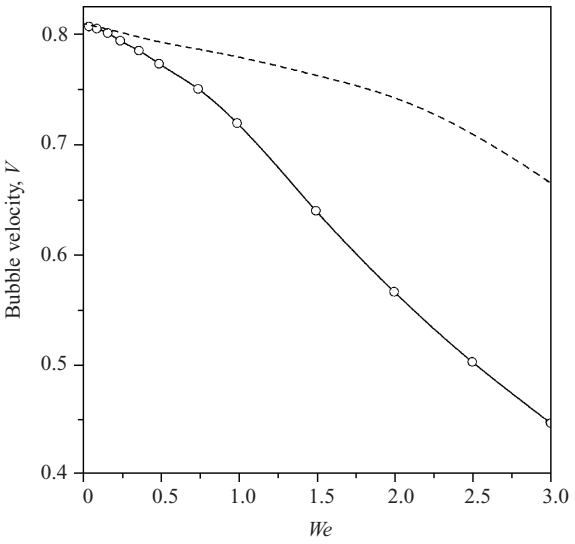

FIGURE 13. Bubble velocity V just prior to touching the other bubble as a function of initial Weber number. The solid line represents the exact calculations while the dashed line corresponds to a spheroidal bubble.

of the increase in the impulse as a result of the flattening which increases their added mass coefficients. Evidently, this increase in the added mass coefficients is not sufficiently great to reduce the bubbles velocity to zero. We see from figure 13 that the relative velocity of the bubbles is reduced by only about 55% even at $We = 3$. This reduction is significantly greater than the reduction of about 18% for spherical bubbles, but not enough to prevent bubbles from coming in contact with each other.

The dashed lines in figures 12 and 13 correspond to an approximate model in which the bubbles are treated oblate spheroids with a variable aspect ratio governed by (3.10). This yields a fairly accurate estimate of the impulse variation with time. The velocity prediction, however, is not accurate. The actual bubbles are more deformed and their shape deviates considerably from an ellipsoid. As a consequence, the added mass coefficients of the actual bubbles is significantly greater than those of model ellipsoids.

From the calculations above, we conclude that two bubbles moving in impurity-free, inviscid liquid will coalesce in a finite time. This was a somewhat unexpected result since it is generally believed that bubbles do not coalesce at sufficiently high Weber numbers. For example, Chesters & Hoffman (1982) performed an analysis of the fluid flow and bubble deformation arising from the collision of two low-Weber-number bubbles in the absence of impurities and found that the bubbles coalesce. However, they speculated that at $O(1)$ Weber numbers, the deformation would be sufficient to produce a bounce. Also, there are at least three sets of experiments that show evidence of bubbles bouncing. The first is experiments by Doubliez (1991) who observed that bubbles rising towards a free surface will bounce off the interface when their Weber number is greater than 0.26. The second is observations by Tsao & Koch (1997) on a rising bubble colliding with a larger bubble held fixed in an inverted tube. These investigators found that the smaller bubble bounced off the fixed bubble for We greater than about 1.8. In both cases the bubbles are bouncing off a gas–liquid interface with much greater surface area and one might suppose that the ability of the interface with large surface area to temporarily store the kinetic energy of the liquid as interfacial energy may be responsible for the observed bounce. In the experiments of Tsao & Koch (1997) the fact that the larger bubble was held fixed might have also played important role in producing the bounce. Finally, Duineveld (1994) has reported observations on pairs of bubble rising side by side which causes an attractive force and brings the bubbles towards each other. He found that larger bubbles with Weber numbers based on their rise velocities greater than about 0.85 bounced while the smaller bubbles coalesced. The Weber number based on relative velocities of the bubbles was greater than 0.18 for bouncing bubbles.

Direct calculations for the geometries considered in the investigations mentioned in the previous paragraph are difficult but hypotheses regarding large surface area and fixed bubble can be partially tested by simulating interaction between a moving bubble and a larger fixed bubble. Figure 14 shows interaction between bubbles of radii a and $3a$. The impulse of the larger bubble was set to zero at all times which amounts to applying a time-varying force on that bubble. This caused the larger bubble to remain nearly fixed at all times. Two cases corresponding to Weber number based on the smaller bubble's velocity and equivalent diameter of 0.5 and 2.0 were simulated. In both cases no bounce occurred as can be seen from figure 14 which shows the shape of the bubbles just prior to touching. For a bounce to occur the impulse of the smaller bubble must become zero and then change sign during the rebound. The potential flow interactions, however, cause the impulse of the smaller bubble to increase with time. Thus we conclude that the observed bounce in the two investigations cited above must be due to physical effects other than those modelled here, i.e. potential flow interaction of bubbles in an impurity-free liquid.

The potential flow approximation can be applied to two colliding bubbles only if the viscous traction exerted by the gas on the liquid film between the bubbles is negligible. Since the velocity gradients in the gas scale with the radial extent of the near-contact region, the viscous stress of the gas will induce velocity variations across

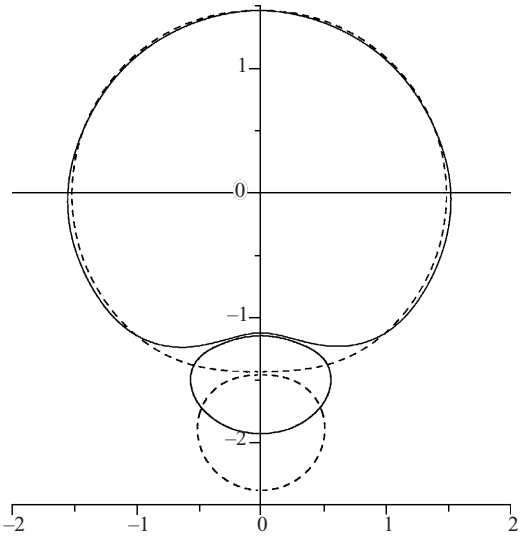

FIGURE 14. Normal collision of two different-sized bubbles with the radii ratio equal to 3.0 for $We = 2.0$ (solid contours) and $We = 0.25$ (dashed contours).

the liquid film if $\mu_g/\mu = O(r_f/h)$ where r_f is the radial extent of the film, h is the film thickness, and μ_g is the viscosity of the gas. At small Weber numbers in the absence of non-hydrodynamic forces, $r_f = O((ah)^{1/2})$ and, since $\mu_g/\mu = O(10^{-3})$, the potential flow approximation holds down to film thicknesses h of order 1 nm. For such a thin film, van der Waals attractions would lead to rapid coalescence. However, at higher Weber numbers, the region of near contact between the bubbles may become larger, so that viscous forces become important at moderate h. For example, if $r_f = 0.5$ mm, then viscous effects would be important for $h \approx 0.5\,\mu$m. It is therefore possible that the bounces observed in Tsao & Koch's and Doubliez' experiments resulted from the finite viscosity of the gas and the bounce coalescence criterion would then depend on Re and μ_g/μ as well as We. The bounce of moderate-Weber-number bubbles rising in a liquid might result from vortex shedding induced by the interaction as suggested by de Vries (2001) in his study of bubble–wall collisions.

4.2. *Bounce in the presence of electrolytes*

We next consider the bounce of bubbles due to presence of non-hydrodynamic repulsive forces between the bubbles. As mentioned earlier, electrolytes such as sodium chloride or magnesium sulphate induce short-range repulsive forces between the bubbles due to hydration effects (Pashley 1981; Lessard & Zieminski 1971; Tsao & Koch 1994). Water molecules strongly associated with large cations such as Na^+ or Mg^{++} adsorbed at the air–water interface are believed to form hydration layers near the interface. Hydration layers are very thin, of the order of a few nanometers. In the present study we shall assume that the non-hydrodynamic pressure induced in the gap between two gas–liquid interfaces separated by distance x is given by

$$p_{nh} = P_0 \exp -(\kappa x) \equiv A\rho V^2 \exp -(Bx/a), \tag{4.1}$$

where P_0 and κ are constants, V is the characteristic velocity used in defining the Weber and Reynolds numbers, and A and B are non-dimensional constants representing the ratio of non-hydrodynamic to hydrodynamic pressures and the inverse of the

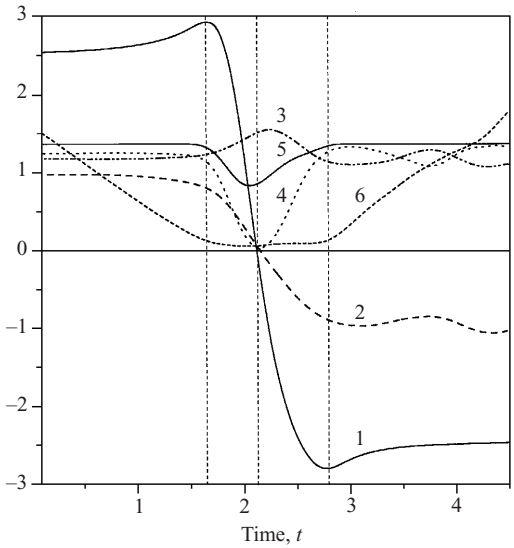

FIGURE 15. Dynamics of a bubble bouncing due to the short-range repulsive force given by (4.1). The curves represent time variation of impulse (line 1), velocity (line 2), aspect ratio (line 3), kinetic energy (line 4), total (kinetic plus excess surface) energy (line 5) and h_{min} (line 6).

distance over which the non-hydrodynamic forces remain significant. The above form of the non-hydrodynamic pressure is chosen such that the pressure remains finite as $x \to 0$, thus permitting the possibility that a bubble–bubble encounter may result in a coalescence when A is not sufficiently large. Since we are primarily interested in bubbles of about 1 mm radius and since κ^{-1} is expected to be of order of few nanometers, the constant B is large. Numerical computations with very large B are extremely difficult but we expect that a reasonable approximation can be obtained by choosing B^{-1} small compared to the extent of bubble deformation which is $O(We^{1/2})$ for small We.

The effect of the non-hydrodynamic pressure is included by simply adding p_{nh} to the right-hand side of the normal-stress condition (2.10). Now as the bubbles approach each other, work must be done against the non-hydrodynamic force and as a result the magnitude of the impulse decreases as the gap between the bubbles decreases. For sufficiently large A the impulse and velocity of the bubbles can be brought to zero before the bubbles touch resulting in the bounce. Figure 15 shows the results for the case of $We = 1$, $A = 20$ and $B = 10$. Curve 1 represents impulse of a bubble as a function of time. We see that the impulse goes through a maximum and a minimum. The time lapse between these two extremas will be referred to as the collision time. The impulse–time curve is not symmetric about the time at which the impulse of the bubble vanishes. This is more clear from curve 2 which shows velocity as a function of time. The oscillations in the velocity after the bounce are more pronounced. Curves 4 and 5 show, respectively, the total kinetic energy of the fluid (translational plus vibrational) and the kinetic energy plus the excess interfacial energy E_s. We see that the minima in the two occur at different times. The minimum in the kinetic plus excess interfacial energy corresponds to roughly 60% of the energy at time $t = 0$. The remaining 40% of the energy was confirmed to equal the work done against the non-hydrodynamic forces. Curve 6 shows the minimum gap thickness between the surfaces of two bubbles as a function of time. It goes through a minimum of $0.05a$

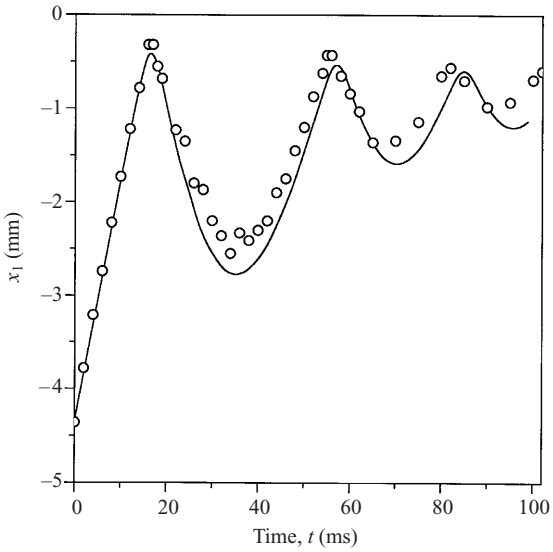

FIGURE 16. Position of centroid as a function of time during its bounce from the horizontal wall. Open circles: observations of Tsao & Koch (1997); solid line: numerical simulations. $a = 0.79$ mm, $Re = 420$, $We = 2.55$ and $Fr = Re/18C_d = 10.25$.

shortly after the bubbles have begun to bounce back. Finally, curve 3 shows aspect ratio of the bubble as a function of time. It goes through a maximum of about 1.5 also just after the bounce begins.

It is interesting to compare the dynamics of the bounce between two bubbles induced by non-hydrodynamic forces with the bounce of a rising bubble from a rigid horizontal wall observed by Tsao & Koch (1997). The velocity of the liquid normal to the wall is zero and this is consistent with an image bubble experiencing a force opposite to gravity. Of course, the potential flow approximation will not be valid very close to the wall where viscous effects are significant and presumably responsible for causing the bounce. For low-Weber-number aerosol drops bouncing from a rigid wall, Gopinath & Koch (2002) showed that a simple non-hydrodynamic repulsive force yields similar drop dynamics to that obtained with a rigorous treatment of the lubricating gas film. This observation for a similar problem supports our use of a non-hydrodynamic force with an image bubble to model the liquid film between a bubble and a wall. Figure 16 shows the position of the centroid of the bubble as a function of time while figure 17 shows the surface area of the bubble as a function of time. The lines represent the results of numerical simulations based on the potential flow approximation together with a non-hydrodynamic force due to an image bubble. The calculations also accounted for viscous effects as described in § 2. The circles in these figures represent the measurements by Tsao & Koch (1997). In making this comparison we chose the radius and the initial aspect ratio of the bubble in our simulations to be the same as those in the experiment. This corresponds to $a = 0.79$ mm, $\chi = 1.8$, $Re = 420$ and $We = 2.55$. These numbers are somewhat different from those reported by Tsao & Koch (1997) but since the viscous drag and other properties are sensitive to the aspect ratio, it is important that the aspect ratio be kept the same as that observed in the experiments. We see that both the computed trajectory and the surface area of the bubble are in excellent agreement with the measured values. Tsao & Koch (1997) have also presented a

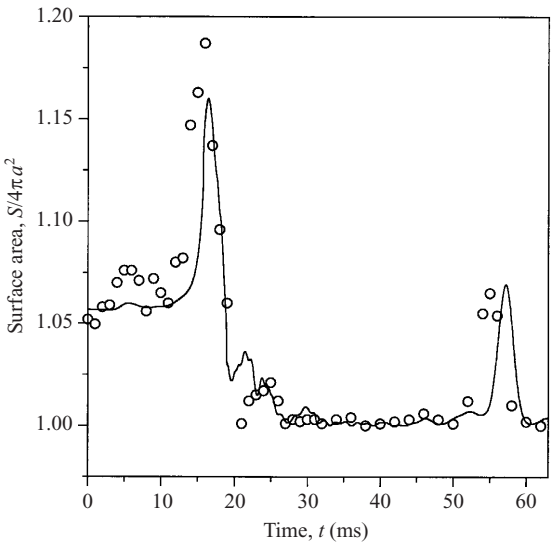

FIGURE 17. Time variation of the normalized surface area $S/4\pi a^2$ of the bubble bouncing from a horizontal solid wall. The open circles represent experimental data of Tsao & Koch (1997), solid line represents the numerical solution. The flow parameters are the same as in figure 16.

sequence of photographs illustrating the shape of the bubble as it approaches and recedes from the wall. The shapes are asymmetric with the wall facing side of the bubble much flatter during the approach than during the rebound. This is also in very good agreement with the results of numerical simulations. Thus, it appears that the potential flow approximation together with non-hydrodynamic repulsive forces from an image bubble models very accurately the collision of a rising bubble with a horizontal wall. It may be noted that Tsao & Koch's experiment used deionized water. The mechanism for the bounce may therefore be quite different than the one modelled in our simulations since one would expect the interaction of the viscous boundary layer at the wall with the bubble to play an important role in the bounce process.

Next, we address two questions: how does the collision time between two bubbles of equal size vary with Weber number when A and B are sufficiently large, and for what values of A and B will the bubbles not bounce? Tsao & Koch (1994) have examined both these questions for the case of small Weber numbers. We shall compare our results with their predictions and provide simple formulas that can be used when the Weber number is not small. For each Weber number we begin with two bubbles initially separated by about 5 radii and determine the times at which the impulses of the bubbles go through extreme values. The collision time, defined as the difference between the times of the two extrema, is evaluated for increasing values of A and B until no significant change in the collision time is noted. For smaller Weber numbers it is necessary to use greater values of A and B since B must be large compared with $We^{-1/2}$ and since the work done by the non-hydrodynamic force is $O(\rho V^2 A/B \exp(-Bh_{min}))$, $h_{min}a$ being the minimum gap between the bubbles. This work must be comparable to the initial kinetic energy of $O(\rho V^2)$ suggesting thereby that A must also be sufficiently large. The numerical computations become challenging as A and B are increased since the time step for integrating the equations of motion for the bubbles must be decreased and N_s, the number of multipoles used

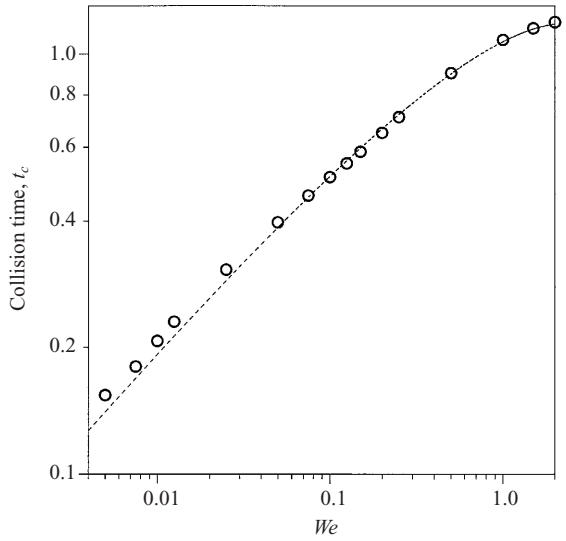

FIGURE 18. Collision time as a function of Weber number obtained from numerical experiments (open circles) for $A = 2000$ and $B = 200$ and given by (4.2) (dashed line).

in determining the velocity potential, must be increased to obtain accurate results. We used N_s in the range of 10–20 depending on the magnitude of B and, for small Weber numbers, the results for collision time as a function of B were extrapolated to estimate the collision time as $B \to \infty$. The results for collision times are shown in figure 18. For small Weber numbers the collision time is proportional to $We^{1/2}a/V$ in agreement with Tsao & Koch's analysis. The dynamic boundary condition dictates that the non-hydrodynamic pressure in the gap between the bubbles during the bounce be $O(\sigma/a)$ in order that a relatively flat liquid film between the two bubbles is formed during the bounce. The radial extent of this region is such that the change in interfacial energy is comparable to the initial kinetic energy of the liquid. This radial extent can therefore be shown to be $O(aWe^{1/4})$ (Tsao & Koch 1994). The force due to non-hydrodynamic pressure therefore equals $O(\sigma aWe^{1/2})$. This force must equal the rate of change of impulse $O(\rho a^3 V/t_c)$ during the bounce, which requires that the collision time t_c be $O(We^{1/2}a/V)$. The results of computations for the collision time are approximated well by the formula

$$t_c = (a/V)(\alpha_1 We^{1/2} - \alpha_2 We^{3/4}) \tag{4.2}$$

with $\alpha_1 = 2.32$ and $\alpha_2 = 1.25$ for $We < 2$.

The calculation of the minimum value of A below which the bubbles will fail to bounce is somewhat more complicated. In principle, one can systematically decrease A while keeping B and We fixed to determine the minimum value of A below which the bubbles coalesce. This calculation, however, is difficult because the accuracy of the solution for flow in the gap between the bubbles deteriorates as the liquid film thickness becomes very small. The bubbles touch each other in some cases after they have reversed their velocities due to large shape oscillations which may have been induced because of the breakdown in the numerical solution for very thin films. To make sure that this bubble overlap did not occur due to time stepping or inaccurate solution, one must use very small time steps and very large N_s. To avoid this, we determine the minimum A for the bounce by a two-step process. For every pair of A,

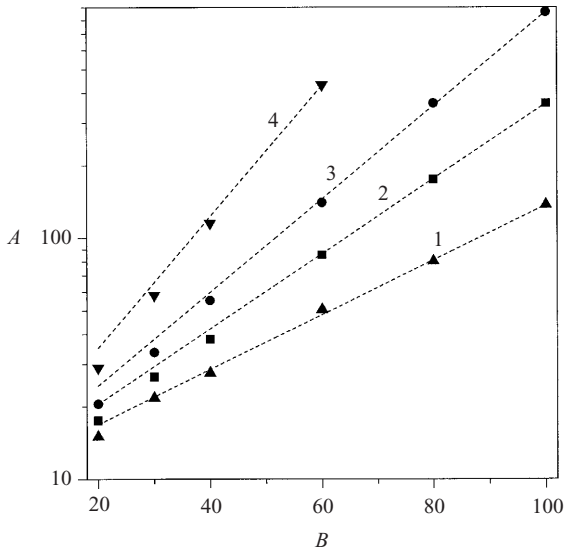

FIGURE 19. A as a function of B for a fixed $h_{min} = 0.01a$ (line 1), $h_{min} = 0.015a$ (line 2), $h_{min} = 0.02a$ (line 3) and $h_{min} = 0.03a$ (line 4); $We = 1.0$

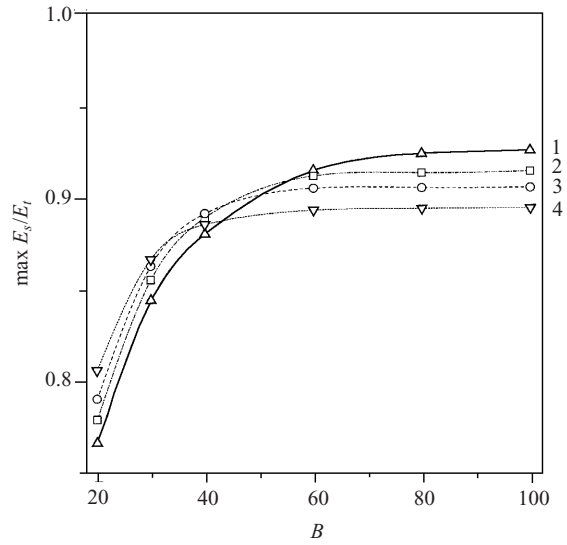

FIGURE 20. Maximum fraction of stored interface energy E_s/E_t during the collision as a function of B. The lines 1–4 are calculated for $h_{min}/a = 0.01$, 0.015, 0.02, and 0.03, respectively.

B for which the bubbles bounce, we can determine the minimum gap $h_{min}a$ for the entire bounce. In the first step, we fix B and vary A until h_{min} from the simulation equals a prescribed value for h_{min}. In the second step, we extrapolate the results obtained for A as a function of h_{min} to $h_{min} = 0$.

Figure 19 shows A as a function of B for selected values of h_{min} for $We = 1$. Figure 20 shows the maximum fraction of total (kinetic + surface) energy stored as interfacial energy during the bounce as a function of B and h_{min}. We see that this fraction approaches a constant as B is increased and that the energy stored as

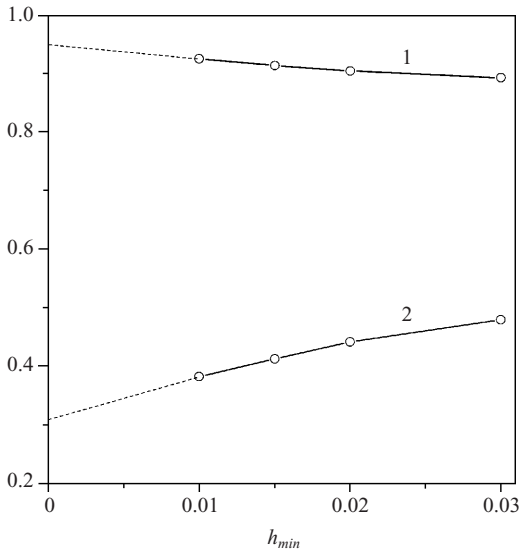

FIGURE 21. E_s/E_t (line 1) and the fitting parameter L (line 2) as a function of h_{min}; solid lines represent numerical data and the dashed lines show an extrapolation as $h_{min} \to 0$.

interfacial energy increases as h_{min}/a decreases. Extrapolating the results to $h_{min} = 0$ (cf. figure 21) we find that more than 90% of the initial kinetic energy is stored as the interfacial energy for the case when the bounce just barely occurs. In other words, nearly all of the initial kinetic energy is converted into interfacial energy for a critical collision, i.e. a collision with $h_{min} \to 0$.

To extrapolate the results to $h_{min} = 0$ we note that the results for A in figure 19 for larger values of B where $\max(E_s)$ has become essentially constant can be fitted according to

$$A = 10 \exp(B/L), \tag{4.3}$$

where L as a function of h_{min} is shown in figure 21. We see that Lh_{min} approaches a constant of about 0.3 as $h_{min} \to 0$. Thus the minimum value of A for bubbles with $We = 1$ to bounce is 10. This procedure is repeated for other Weber numbers and the results for the minimum value of A as a function of We are shown in figure 22. These results for the minimum value of A to prevent coalescence are fitted well by

$$A_{min} = \frac{P_{0,min}}{\rho V^2} = 10.8 + 1.6/We. \tag{4.4}$$

One final remark regarding the results for A_{min} concerns the result for $We = 1$ which is seen to give A_{min} lower than that given by (4.4). For $We \leqslant 0.8$ we found that $h_{min}(t)a$, the minimum distance between the surfaces of the bubbles as a function of time, went through a single minimum during the bounce process, referred to as $h_{min}a$ earlier. At $We = 1$, the film between the bubbles became wavy and h_{min} goes through several local minima as bubble shape oscillations became significant. It is difficult to determine the flow in the gap between the bubbles when this occurs and this may lead to some uncertainty in our estimate of A_{min} for $We = 1$.

4.3. *Pair of rising bubbles*

Next we consider the motion of two bubbles rising due to gravity. Biesheuvel & van Wijngaarden (1982) have determined the trajectories of two equal size spherical

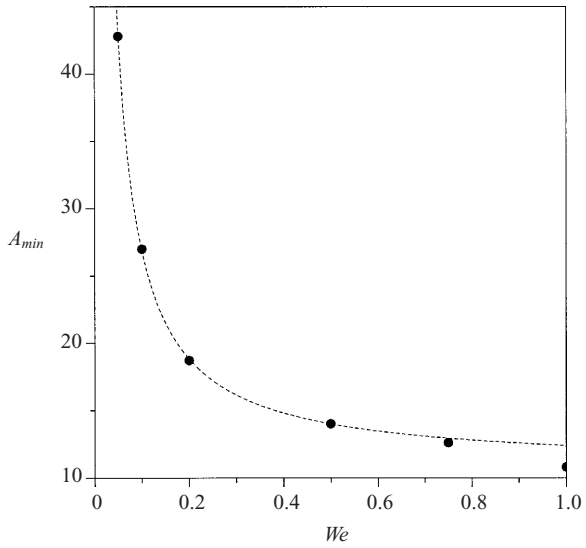

FIGURE 22. Minimum value of A to prevent coalescence as a function of Weber number obtained numerically (solid circles) and approximated by (4.4) (dashed line).

bubbles. They found that when the line joining the initial position of the two bubbles makes an angle with gravity that is greater than $\cos^{-1}(1/\sqrt{3}) = 55°$, the attractive force caused by potential flow interactions would bring the bubbles close to each other. As shown in Sangani & Didwania (1993*b*) and Smereka (1993) this leads to the formation of clusters in bubbly liquids. We have evaluated the trajectories of pairs of bubbles at finite Weber numbers and found that this tendency to form clusters will persist at finite Weber numbers also. As shown in figure 23(a, b) the critical angle for the two bubbles to be attracted towards each other is 55° and 54° for We of respectively 0.5 and 1.5. In other words the critical angle is a very weak function of We. Duineveld (1994) made observations on a pair of bubbles rising through a liquid. He found that bubbles with radius of about 0.86 mm or greater rising through water were first attracted to each other but after one or two bounces separated from each other permanently. It was suggested that the shedding of vortices by the rising bubbles might be responsible for this behaviour, a phenomenon not modelled by the present analysis.

Another related calculation is the interaction of a rising bubble with an inclined wall. Tsao & Koch (1997) observed that when the wall is inclined at an angle greater than 55° with the vertical, the bubble undergoes repeated bounces of nearly equal magnitude. For smaller angles the bubble essentially slides along the wall after the first few bounces of diminishing magnitude. We examined if this phenomenon can be modelled by a leading-order potential flow interaction with an image bubble, non-hydrodynamic repulsive force, and small viscous effects around the surface of each bubble as in the case of bounce from a horizontal wall described earlier. We found that a bubble undergoes bounces of diminishing magnitude and essentially slides along the wall for all inclinations of the wall. We conclude therefore that the interaction with an inclined wall cannot be modelled adequately using the potential flow model. Recently, de Vries (2001) visualized the liquid flow near a bubble colliding with a wall and showed that a vortex was shed behind the bubble when it hit the

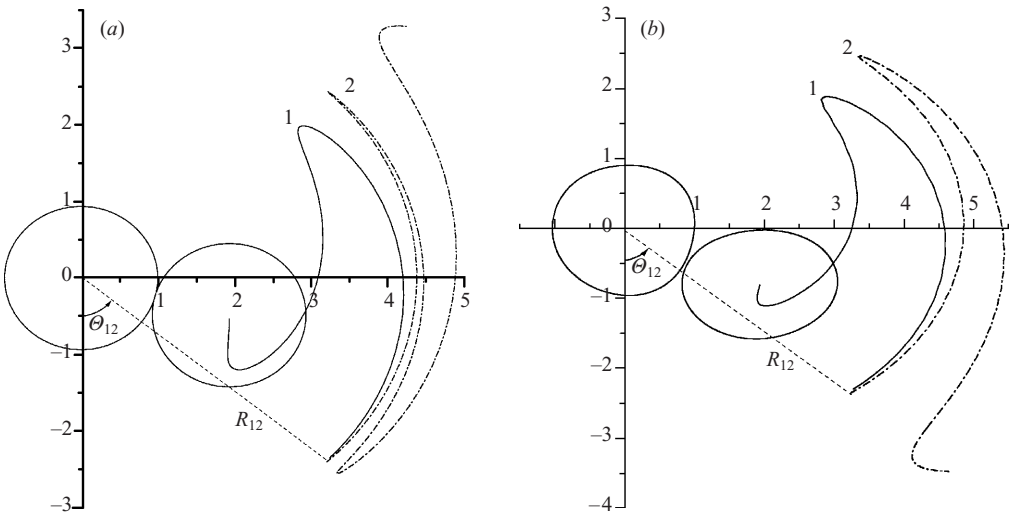

FIGURE 23. (*a*) Trajectories (relative centroid positions) of two rising deformable bubbles at $We = 0.5$. Initial distance between the centroids $R_{12} = 4.0a$; initial angle $\Theta = 54°$ (solid line) and $\Theta = 53°$ (dash-dotted line). (*b*) Trajectories of two rising deformable bubbles at $We = 1.5$. $R_{12} = 4.0a$; initial angle $\Theta = 55°$ (solid line) and $\Theta = 54°$ (dash-dotted line).

wall. He developed a model describing the trajectory of the bubble resulting from this vortical flow.

5. Random arrays of bubbles

We now consider random arrays of bubbles. Our goal is to determine average properties such as the added mass coefficient and viscous drag coefficient as functions of the volume fraction of the bubbles and their aspect ratio. These properties depend on the spatial and velocity distributions of bubbles, which, in turn, depend on the nature of the imposed flow. Rather than carrying out full scale dynamic simulations to determine the spatial and velocity distributions for specific macroscopic imposed flows, we shall restrict our analysis to a simple case in which all bubbles have equal velocities and aspect ratios and are aligned in the direction of the bubbles velocity. Moreover, the bubbles will be taken to be oblate spheroids and their spatial distribution will be taken to be the same as that of non-overlapping (hard) oriented ellipsoids obtained using a suitable molecular dynamics code.

As in most studies, random arrays will be modelled as periodic arrays with each unit cell containing N bubbles, N being sufficiently large so that the average properties are nearly independent of N. The expression for the velocity potential given earlier is modified to account for the periodic images of the N bubbles in the primary unit cell. The boundary condition $\boldsymbol{n} \cdot \nabla\phi = \boldsymbol{n} \cdot \boldsymbol{V}$ on the surface of the bubbles is satisfied in the integral sense by multiplying it with ellipsoidal surface harmonics and integrating over the surface of the bubble. With the integral determined from the velocity or potential at P points on the surface of a bubble, and with the flow induced by each bubble represented by $N_s(N_s + 2)$ multipoles, we need to carry out computations of $O(N_s^2 P N^2)$. The $O(N)$ algorithm described by Sangani & Mo (1996) can be used alternatively to reduce the computations to $O(N_s^4 P N)$. The unit cell is divided into an $O(PN)$ number of small boxes and the ellipsoidal multipoles due to each bubble are

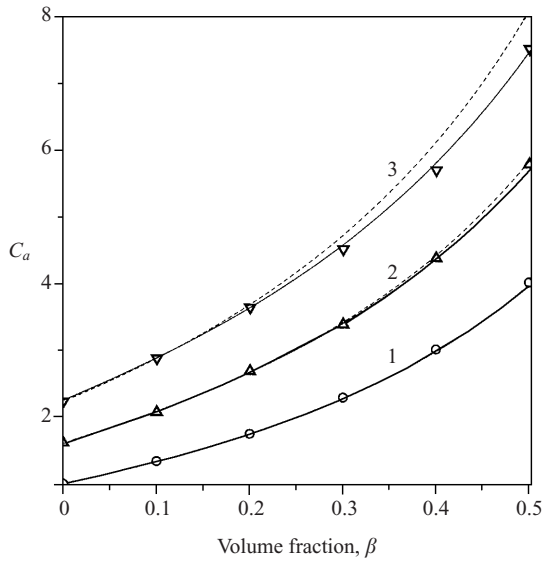

FIGURE 24. Added mass coefficient C_a as a function of a volume fraction β of randomly distributed spherical (line 1) and spheroidal (lines 2 and 3) bubbles. The points represent the results of numerical simulation for $\chi = 1$ (open circles), $\chi = 1.5$ (triangles) and $\chi = 2.0$ (upper triangles). The dashed lines represent the effective-medium approximation and the solid lines the fitting by (5.3).

expressed in terms of equivalent spherical multipoles at the centre of the box in which the centre of a bubble lies. These equivalent spherical multipoles are re-expanded to equivalent multipoles of bigger boxes. This and subsequent steps are described in detail in Sangani & Mo (1996). The only modification needed for the present case is the expansion of ellipsoidal multipoles into equivalent spherical multipoles. The formulas needed for this purpose are given in the Appendix. We found that $N = 32$ and $N_s = 6$ were sufficient to determine the average properties accurately.

The results for added mass and viscous drag coefficients obtained by averaging over 30 configurations for each β and χ are shown in figures 24 and 25, β being the volume fraction of bubbles. These coefficients are defined by

$$\langle \boldsymbol{I} \rangle = m[C_a(\boldsymbol{V} - \langle \boldsymbol{u} \rangle)/2 - \langle \boldsymbol{u} \rangle], \tag{5.1}$$

$$\langle \boldsymbol{F}_v \rangle = 12\pi\mu a C_d(\langle \boldsymbol{u} \rangle - \boldsymbol{V}). \tag{5.2}$$

The gas–liquid mixture velocity $\langle \boldsymbol{u} \rangle$ was taken to be zero.

The results for the added mass coefficient can be fitted according to the simple formula

$$C_a = \frac{1 + 2\beta}{1 - \beta} + (\chi - 1)(5/4 + 3\beta + 6\beta^3). \tag{5.3}$$

The solid lines in figure 24 correspond to the above formula. The first term on the right-hand side corresponds to the added mass coefficient for a spherical bubble ($\chi = 1$) (Zuber 1964; Sangani, Zhang & Prosperetti 1991). The coefficient 5/4 corresponds to the result for an isolated bubble with an aspect ratio not much greater than unity.

The dashed lines in figure 24 correspond to predictions of an effective-medium theory which uses a simple model for determining the conditionally averaged fields as described below.

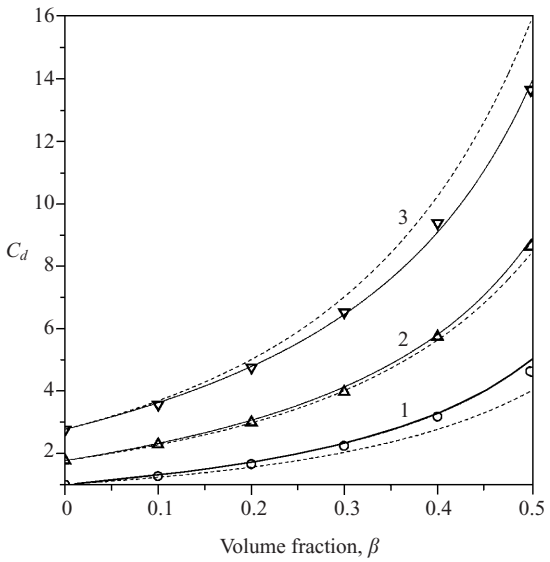

FIGURE 25. As figure 24 but for viscous drag coefficient C_d. The solid lines are the fitting curves defined by (5.14).

Defining the potential inside the bubbles such that ϕ is continuous across the surface of the bubbles, taking the velocity inside the bubble to equal $\boldsymbol{V}$, and ensemble-averaging the relation between the velocity and velocity potential with the positions of p bubbles fixed yields

$$\langle \boldsymbol{u} \rangle_p = \nabla \langle \phi \rangle_p + \langle g(\boldsymbol{V} - \nabla \phi^G) \rangle_p, \tag{5.4}$$

where g is the gas phase indicator defined to equal unity for a point inside the bubble and zero for a point in the liquid phase. Note that the velocity inside the bubble is not given by $\nabla \phi^G$ since the potential flow satisfies the boundary condition for only the normal component of velocity. We introduce the closure

$$\langle g(\boldsymbol{V} - \nabla \phi^G) \rangle_0 = \alpha \beta (\boldsymbol{V} - \langle \boldsymbol{u} \rangle_0), \tag{5.5}$$

where the constant α is to be determined by solving for the conditionally averaged velocity. The effective-medium theory employs a similar closure relation for the conditionally averaged field outside a suitably defined exclusion region around a single, fixed bubble referred to as the effective medium. Thus, we take

$$\langle g(\boldsymbol{V} - \nabla \phi^G) \rangle_1 = \alpha \beta (\boldsymbol{V} - \langle \boldsymbol{u} \rangle_1) \tag{5.6}$$

in the effective medium, the quantity on the left-hand side being set to zero for all points in the exclusion region.

For spherical bubbles of radius unity the exclusion region is usually chosen to be spherical so that for $1 \leqslant r \leqslant R$ the velocity potential satisfies the equations for pure liquid, and for $r \geqslant R$ the potential satisfies the effective-medium equations such as (5.6). The most common choices for R are unity and $\beta^{-1/3}$. In recent years a choice $R^3 = (1 - S(0))/\beta$, where $S(0)$ is the zero wavenumber structure factor, which matches the total exclusion region in the actual suspension to the one in the effective-medium approximation, has also been shown to yield quite accurate estimates of the effective properties (Spelt *et al.* 2001). For added mass and viscous drag coefficients for

spherical bubble suspensions the simple choice $R = \beta^{-1/3}$ gives reasonably accurate estimates.

For oblate spheroidal bubbles it is natural to take the exclusion region to be also an oblate spheroid with a total volume that is β^{-1} times the volume of the bubbles. Two simple choices for the shape of this exclusion region correspond to (i) an exclusion oblate spheroid having the same aspect ratio as the bubbles and (ii) an oblate spheroid that is confocal to the bubble. The aspect ratio of the exclusion region in the latter case is not the same as the aspect ratio of the bubble. Instead, the focal plane radii d for the bubble and the excluded region are equal. The outer confocal ellipsoid would approach the spherical shape as $R \to \infty$. We carried out effective-medium calculations for both of the above cases. The analysis for the first is very involved since the oblate spheroidal coordinate systems for two oblate spheroids of equal aspect ratio but unequal sizes are different and, as a consequence, the expression for the velocity potential written in one system must be re-expanded in the other to satisfy the boundary conditions. This leads to an infinite set of equations that must be solved to determine the added mass coefficient of the bubble. The analysis for the second, on the other hand, is much easier, and in fact gives estimates that are in better agreement with the simulation results. We therefore give the results corresponding only to case (ii) here.

Taking the bubble velocity to be along the x_1-axis and the mean mixture velocity $\langle \boldsymbol{u} \rangle_0 = \boldsymbol{0}$, the velocity potential in the exclusion region is expressed as

$$\langle \phi \rangle_1 = A_{10} F_1^0(\boldsymbol{x}, d) + a_{10} f_{10}(\boldsymbol{x}, d), \qquad \bar{\xi}_0 \leqslant \bar{\xi} \leqslant \bar{\xi}_1, \tag{5.7}$$

where

$$f_n^m(\boldsymbol{x}, d) = P_n^{-m}(\mathrm{i}\bar{\xi}) P_n^m(\eta)\, \mathrm{e}^{\mathrm{i}m\varphi} \tag{5.8}$$

are the regular solid spheroidal harmonics and $d^3 \bar{\xi}_1 \xi_1^2 = \beta^{-1}$ in order that the exclusion region corresponds to an oblate spheroid of volume β^{-1} times that of the bubble. In particular, $f_1^0(\boldsymbol{x}, d) = x_1/d$; the velocity potential in the effective medium is expressed as

$$\langle \phi \rangle_1 = G x_1 + A'_{10} F_1^0(\boldsymbol{x}, d), \quad \bar{\xi} > \bar{\xi}_1, \tag{5.9}$$

with $G = \| \langle \nabla \phi \rangle_0 \| = \alpha \beta V$. The constant α can be shown to be related to A_{10} by

$$\alpha = d^2 A_{10}/V. \tag{5.10}$$

The velocity in the effective medium is given by

$$\langle \boldsymbol{u} \rangle_1 = \frac{1}{1 - \alpha\beta} \nabla(\langle \phi \rangle_1 - G x_3). \tag{5.11}$$

Now the continuity of $\langle \varphi \rangle_1$ and $\langle \boldsymbol{u} \rangle_1 \cdot \boldsymbol{n}$ at $\bar{\xi} = \bar{\xi}_1$ yields $A'_{10} = 0$ and using the condition that $\boldsymbol{n} \cdot \nabla \langle \varphi \rangle_1 = \boldsymbol{n} \cdot \boldsymbol{V}$ at the surface of the bubble we obtain

$$\frac{d^2 A_{10}}{V} = \alpha = \frac{-d^3}{[Q_1^{0\prime}(\bar{\xi}_1) - Q_1^{0\prime}(\bar{\xi}_0)]}. \tag{5.12}$$

The added mass coefficient can be shown to be related to α by

$$C_a = -2 - 2\alpha. \tag{5.13}$$

As seen in figure 24, the above effective-medium theory gives estimates of the added mass coefficients that are only slightly greater than the results of numerical simulations. The effective-medium theory based on an exclusion region having the same

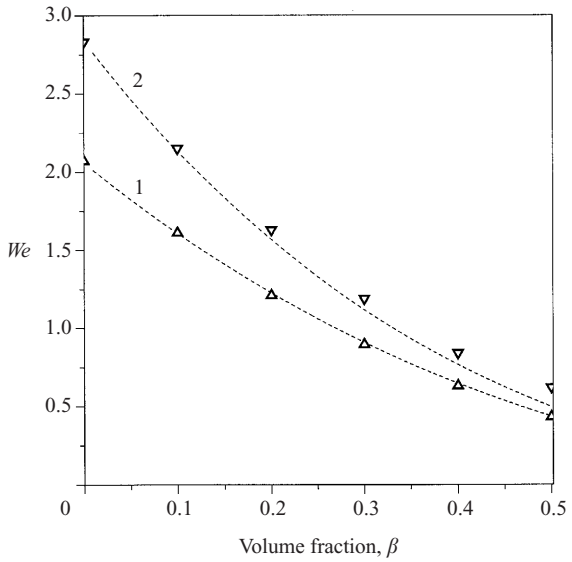

FIGURE 26. Weber number We as a function of a volume fraction β of randomly distributed spheroidal bubbles. The points represent the results of numerical simulation for $\chi = 1.5$ (triangles) and $\chi = 2.0$ (upper triangles), the dashed lines represent the effective-medium approximation.

aspect ratio as the bubble on the other hand gave substantially lower estimates of the added mass coefficient. The effective-medium theory based on the model of confocal spheroids effectively assumes fewer bubble pairs aligned in the direction of the bubble velocity compared with the exclusion region based on equal aspect ratio. Since the added mass of a pair of bubbles oriented along the bubbles' velocity direction is smaller than the added mass of a pair aligned perpendicular to the velocity, we expect the added mass coefficient based on the equal-aspect-ratio model to be lower than that based on equal confocal radii. Finally, we should mention that the effective medium using the confocal spheroids described here was first presented by Smereka & Milton (1991). Although these investigators did not present their derivation in terms of conditionally averaged fields, the final result they derived is the same as obtained here.

Figure 25 shows numerical results for the viscous drag coefficient as a function of aspect ratio and volume fraction. The solid lines correspond to

$$C_d(\beta, \chi) = C_d(0, \chi)(1 + 4\beta/3)/(1 - 4\beta/3) \tag{5.14}$$

whereas the dashed lines correspond to the predictions of a confocal-spheroids effective-medium approximation. The ratio of viscous drag coefficients at finite β and $\beta = 0$ is related to the ratio of the square of A_{10}, i.e.

$$\frac{C_d(\beta, \chi)}{C_d(0, \chi)} = \left(\frac{A_{10}(\beta, \chi)}{A_{10}(0, \chi)}\right)^2. \tag{5.15}$$

The above expressions allow one to estimate the added mass and viscous drag coefficients given β and the aspect ratio of the bubbles. In practice, the aspect ratio is not known *a priori* and therefore we need an additional relation among Weber number, β and χ. To determine an aspect ratio, we used the same procedure as in § 3 (namely, Moore's single bubble analysis). The results of numerical simulations are given in figure 26. The dashed lines represent the relationship obtained from the

effective-medium approximation which yields

$$We = \frac{4(1+\chi^2-2/\chi)}{\chi^{1/3}\alpha^2}. \tag{5.16}$$

We note that the effective-medium theory describes fairly accurately the relationship among We, χ and β. We also note that, since the viscous drag coefficient is proportional to α^2, we have

$$\frac{We(\beta,\chi)}{We(0,\chi)} = \frac{C_d(0,\chi)}{C_d(\beta,\chi)}. \tag{5.17}$$

Recently, Zenit *et al.* (2001) have presented data on bubbles rising through water containing some magnesium sulphate which inhibits coalescence. The expression for the viscous drag coefficients and aspect ratio as a function of volume fraction and Weber number were not available then and hence the investigators compared their experimental data with those obtained by combining the theory for spherical bubbles (Spelt & Sangani 1998) with a single oblate spheroidal bubble (Moore 1965). With the dependence among various variables determined here we are in a slightly better position to compare the theory of motion of bubbles based primarily on the potential flow approximation with that observed in the experiments. Our calculations were carried out for a hard-oblate spheroid distribution of bubbles whereas the experiments showed some evidence of clustering of bubbles in the plane normal to gravity. Zenit *et al.* (2001) have measured the variance in the velocities of bubbles. Their data are fitted well by the expression

$$A \equiv \frac{V^2}{T} = (0.02+0.5\beta)^{-1}, \tag{5.18}$$

where $3T$ is the bubble-phase velocity variance. For spherical bubbles Spelt & Sangani (1998) found that the viscous drag coefficient for a bubble suspension with finite A was greater than the viscous drag coefficient of a bubble suspension with a hard-sphere spatial and uniform velocity distribution having the same volume fraction β by a factor of $1+(3/20)A\beta$. Accordingly, we take

$$C_d(A,\beta,\chi) = C_d(\beta,\chi)(1+3A\beta/20) \tag{5.19}$$

with $C_d(\beta,\chi)$ given by the effective-medium theory described above. It should be noted that the velocity variance affects the viscous drag coefficient and other properties of bubble suspensions in two ways. First, is the direct effect of velocity variance for a given spatial distribution of bubbles. It is found that this direct effect is relatively insignificant, at least for the case of spherical bubbles (Sangani *et al.* 1991). The added mass and viscous drag coefficients of bubbles having the same spatial distribution vary only slightly as the velocity variance is increased from zero to infinity. The second is the indirect effect of changing the spatial distribution of bubbles. The spatial distribution approaches a random distribution when the velocity variance is much greater than the square of mean bubble velocity and therefore the hard-oblate ellipsoid spatial distribution used in the simulations presented here corresponds roughly to $A=0$. The clustering is increased as A is increased and it is this indirect effect that is more significant and accounted for by (5.19). Lower velocity variances generally lead to greater clustering and hence higher added mass and viscous drag coefficients. Likewise, the Weber number is modified as given by

$$We(A,\beta,\chi) = We(\beta,\chi)/(1+3A\beta/20) \tag{5.20}$$

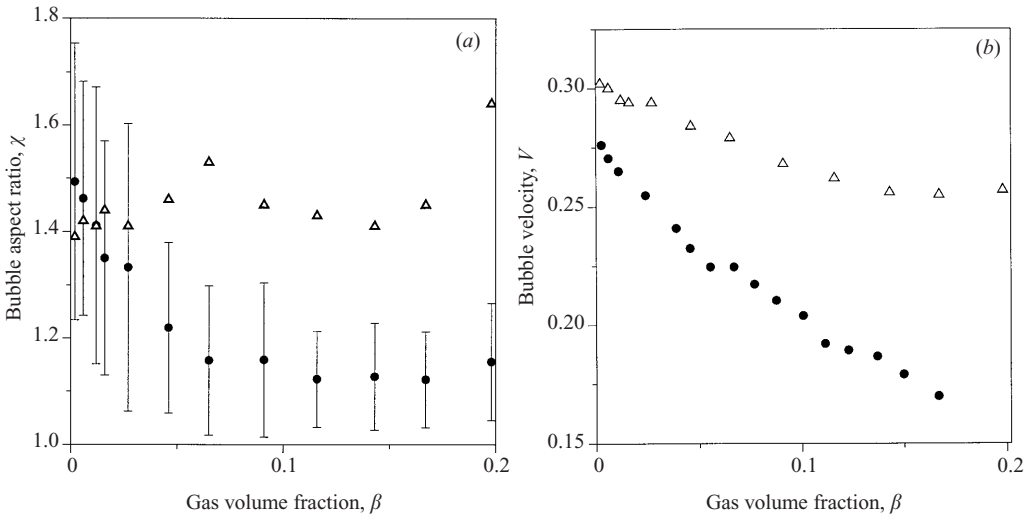

FIGURE 27. (*a*) Bubble aspect ratio as a function of gas volume fraction. Comparison with the experiments of Zenit *et al.* (2001); circles represent experimental data and the triangles the theory. (*b*) Bubble rise velocity as a function of gas volume fraction. Comparison with the experiments of Zenit *et al.* (2001) circles represent the experiments and triangles the theory.

with, once again, $We(\beta, \chi)$ representing the Weber number given by the effective-medium theory.

The mean bubble velocity V is given by

$$V = \frac{a^2 g}{9\mu C_d(A, \beta, \chi)} = \left(\frac{\sigma We(A, \chi, \beta)}{2a}\right)^{1/2}, \tag{5.21}$$

where the second equality follows directly from the definition of the Weber number. The above equations can be solved simultaneously for given values of A, β and a to determine V and χ. The mean liquid velocity was zero in the experiments and therefore the rise velocity and gas–liquid mixture average velocities are given by

$$W = V/(1-\beta), \quad \langle u \rangle = \beta W = \beta V/(1-\beta). \tag{5.22}$$

Figures 27*a* and 27*b* show comparisons between the estimates for W and χ obtained by the above scheme with those reported by Zenit *et al.* (2001). Calculations were done with $\mu = 10^{-3}$ Pa s, $g = 9.81\,\mathrm{m\,s^{-2}}$ and $\sigma = 0.07\,\mathrm{N\,m^{-1}}$. The mean radius of the bubbles varied in the experiment with the volume fraction of bubbles, from about 0.67 mm to 0.75 mm. The computed values of W and χ corresponded to the measured value of a for each β. We see that both the aspect ratio and the rise velocity predicted from the theory are considerably greater than the measured values. The rise velocity is highly sensitive to a and σ. A value of $0.05\,\mathrm{N\,m^{-1}}$ for σ, for instance, would lower the rise velocity but increase further the discrepancy between the measured and predicted aspect ratios since the aspect ratio increases with the decrease in the interfacial tension. The dependence on the radius is even stronger and it is possible to decrease both W and χ by reducing a but this would require that a decrease significantly with β in contradiction with the measurements, which show very clearly that the radius of the bubbles increases with increasing β.

One plausible cause of the observed discrepancy between the theory and experiments is the wall effects. The rise velocity of an isolated bubble in a large container was found

to be $0.32\,\mathrm{m\,s^{-1}}$ while the average rise velocity for a very dilute bubbly liquid (β less than 10^{-4}) was about $0.29\,\mathrm{m\,s^{-1}}$ for the 2 cm wide channel in which the experimental data reported in figure 27 were taken. The data for β greater than 0.001 extrapolated to $\beta = 0$ yields an even lower value of about $0.275\,\mathrm{m\,s^{-1}}$. In other words, the velocity calculated from Moore's expression is about 16% greater than the measured value obtained by extrapolating the data to $\beta = 0$. Van Wijngaarden & Kapteyn (1990) note about 18% difference for their data taken with about twice the bubble size and a 8 cm diameter pipe. Zenit *et al.* (2001) observed that bubbles tend to slow down considerably near the wall and tend to make a sideways motion from one side of the container to the other side in very dilute bubbly liquids. Flow visualizations by de Vries (2001) for about 0.9 mm bubbles interacting with a wall show evidence of vortex shedding. Even putting aside this sideways motion and vortex shedding, which clearly cannot be modelled with the potential flow approximation, we note that the rise velocity in a channel of finite wall thickness will differ from that in an infinite suspension having the same spatial and velocity distribution by a factor of $O(a^2/H\delta)$ or $O(aRe^{1/2}/H)$ due to energy dissipation in the boundary layers at walls. Here, H is the width of the channel and δ is the characteristic boundary layer thickness at the wall. This estimate is obtained by assuming that the energy dissipation per unit surface area of the wall is $O(\mu\langle u^2/\delta\rangle)$ and that the liquid velocity variance near the wall equals that in potential flow of dilute bubbly liquids, i.e. $\langle u^2\rangle \sim \beta V^2$ (Biesheuvel & van Wijngaarden 1982). The ratio $aRe^{1/2}H$ is about 0.7 for Zenit *et al.*'s (2001) experiments and about 1.5 in van Wijngaarden & Kapteyn's experiments if we take H as the ratio of volume to surface area of the container. The observed discrepancy between the data for very dilute bubbly liquids and bubbly liquids with β greater than say 10^{-3} might have resulted from the wall–bubble interactions mentioned earlier which greatly enhanced the liquid velocity variance as noted by Zenit *et al.* (2001) and which, in turn, might have led to additional viscous dissipation at the walls. Finally, it may be noted that the data for both the rise velocity and aspect ratio as functions of β can be fitted very well by multiplying C_d in (5.21) by $1 + \alpha(aRe^{1/2}/H)$ with $\alpha = 0.4/(1-3\beta)^3$.

6. Summary

A numerical method for simulating the motion of finite-Weber-number potential flow induced by the motion of bubbles is described. The method uses ellipsoidal harmonics to represent the shape of the bubbles and the velocity induced by the bubbles together with an $O(N)$ algorithm for computing flows induced by a distant group of bubbles. The method is applied to study several problems involving one, two, or many bubbles. The results obtained would be useful in establishing an analytical framework for developing equations of motion of finite-Weber-number bubbly liquids.

This work was supported by NASA under grant number NAG3-1853.

Appendix. Translation of Laplace singularities

The only part of the $O(N)$ algorithm by Sangani & Mo (1996) to be modified in the case of deformable bubbles is the translation of singularities. We need the formulas providing the translation of the potential field ϕ_c with its singularities at $\boldsymbol{x}_c$ to an equivalent field ϕ_p with its singularities at $\boldsymbol{x}_p$ such that both ϕ_c and ϕ_p and their derivatives have the same value at the points $\boldsymbol{x}$ far from both $\boldsymbol{x}_c$ and $\boldsymbol{x}_p$. Let S_t^s and

s_t^s denote, respectively, the singular and regular solid spherical harmonics:

$$S_t^s(\boldsymbol{x}) = \frac{(t-s)!}{r^{t+1}} P_t^s(\mu)\exp(\mathrm{i}s\varphi), \quad s_t^s(\boldsymbol{r}, d) = \frac{r^t}{(t+s)!} P_t^s(\mu)\exp(\mathrm{i}s\varphi). \tag{A 1}$$

The expression for translating singularities given in Sangani & Mo (1996) is modified to

$$S_t^s(\boldsymbol{x}-\boldsymbol{x}^c) = \sum_{k=t}^{\infty}\sum_{l=-k}^{k}(-1)^{t+k+s+l} s_{k-t}^{s-l}(\boldsymbol{x}^{pc}) S_k^l(\boldsymbol{x}-\boldsymbol{x}^p) \tag{A 2}$$

provided that $\|\boldsymbol{x}-\boldsymbol{x}^p\| > \|\boldsymbol{x}^{pc}\|$, where $\boldsymbol{x}^{pc} = \boldsymbol{x}^p - \boldsymbol{x}^c$.

To obtain the analogous translation formulas for a solution written in terms of singular spheroidal harmonics (2.14)–(2.15), we start with the expansion (Kushch 1998)

$$F_n^m(\boldsymbol{x}, d) = (-1)^m \sum_{t=n}^{\infty}{}' K_{nt}(d) S_t^m(\boldsymbol{x}), \tag{A 3}$$

valid for $\|\boldsymbol{x}\| > d$. The prime means that the sum contains only the terms with $(n-t)$ even and

$$K_{nt}(d) = (-1)^{(t-n)/2}\sqrt{\pi}\left(\frac{d}{2}\right)^{t+1} \Big/ \Gamma\left(\frac{t+n}{2}+\frac{3}{2}\right) \Big/ \left(\frac{t-n}{2}\right)! \tag{A 4}$$

for $t-n$ even and $K_{nt}(d) = 0$ otherwise. Combining (A2) and (A3) and using the summation rule

$$\sum_{t=n}^{\infty}{}' \sum_{k=t}^{\infty}\sum_{l=-k}^{k} = \sum_{k=n}^{\infty}\sum_{l=-k}^{k}\sum_{t=n}^{k}{}' \tag{A 5}$$

we obtain

$$F_n^m(\boldsymbol{x}-\boldsymbol{x}^c, d) = \sum_{k=n}^{\infty}\sum_{l=-k}^{k} \beta_{nk}^{ml} S_k^l(\boldsymbol{x}-\boldsymbol{x}^p), \tag{A 6}$$

where

$$\beta_{nk}^{ml} = (-1)^{n+k+l} \sum_{t=n}^{k}{}' K_{nt}(d) s_{k-t}^{m-l}(\boldsymbol{x}^{pc}) \tag{A 7}$$

is a finite sum. Expansion (A6) is convergent for $\|\boldsymbol{x}-\boldsymbol{x}^p\| > \|\boldsymbol{x}^{pc}\|$ and $\|\boldsymbol{x}-\boldsymbol{x}^c\| > d$. As easily seen, satisfaction of both these conditions is provided by the scheme of an $O(N)$ algorithm. Application of (A6) to (2.14) gives us

$$\sum_{c=1}^{N}\sum_{n=1}^{\infty}\sum_{m=-n}^{n} A_{nm}^{(c)} F_n^m(\boldsymbol{x}-\boldsymbol{x}^c, d) = \sum_{k=1}^{\infty}\sum_{l=-k}^{k} B_{kl}^{(p)} S_k^l(\boldsymbol{x}-\boldsymbol{x}^p) \tag{A 8}$$

where

$$B_{kl}^{(p)} = \sum_{n=1}^{k}\sum_{m=-n}^{n} \beta_{nk}^{ml} A_{nk}^{(c)}. \tag{A 9}$$

The formulas (A6) and (A7) are sufficient to perform the transformation in the case of aligned local and global coordinate systems. In the general case of arbitrarily oriented local coordinate systems the local and global coordinates are related by (2.4) and, hence, additional effort is needed to accomplish translation of singularities. From

(2.4), $\boldsymbol{y}^c = \boldsymbol{O}_c^T \cdot (\boldsymbol{x} - \boldsymbol{x}^p)$; so, the problem is to represent $F_n^m(\boldsymbol{O}_c^T \cdot (\boldsymbol{x} - \boldsymbol{x}^c), d)$ in terms of $S_k^l(\boldsymbol{x} - \boldsymbol{x}^p)$.

To this end, we apply first the formula (A3), with argument $\boldsymbol{O}_c^T \cdot (\boldsymbol{x} - \boldsymbol{x}^c)$. Next we make use the relation

$$S_t^m(\boldsymbol{O} \cdot \boldsymbol{x}) = \sum_{s=-t}^{t} H_{2t}^{t-m,t-s}(\boldsymbol{w}) S_t^s(\boldsymbol{x}), \tag{A 10}$$

where $H_t^{s,l}$ are the spherical harmonics in a four-dimensional space (see e.g. Bateman & Erdeyi 1953) and $\boldsymbol{w} = \{w_1, w_3, w_3, w_4\}$, $\|\boldsymbol{w}\| = 1$ is the vector determining uniquely the rotation matrix

$$\boldsymbol{O} = \begin{pmatrix} w_2^2 - w_1^2 - w_3^2 + w_4^2 & 2(w_2 w_3 - w_1 w_4) & 2(w_1 w_2 + w_3 w_4) \\ 2(w_2 w_3 + w_1 w_4) & w_3^2 - w_1^2 - w_2^2 + w_4^2 & 2(w_1 w_3 - w_2 w_4) \\ 2(w_1 w_2 - w_3 w_4) & 2(w_1 w_3 + w_2 w_4) & w_1^2 - w_2^2 - w_3^2 + w_4^2 \end{pmatrix}. \tag{A 11}$$

Finally, application of (A2) and summation rule (A5) gives us again (A6) with $F_n^m = F_n^m(\boldsymbol{O}_c^T \cdot (\boldsymbol{x} - \boldsymbol{x}^c), d)$ and

$$\beta_{nk}^{ml} = (-1)^{n+k+m+l} \sum_{t=n}^{k} {}'K_{nt}(d) \sum_{s=-t}^{t} (-1)^s H_{2t}^{t-m,t-s}(\boldsymbol{w}_c) s_{k-t}^{s-l}(\boldsymbol{x}^{pc}). \tag{A 12}$$

The geometrical restrictions on using the expansion (A6) with the coefficients (A12) are the same as in the case of aligned coordinate systems.

Now, one final remark. Meiron (1989) found that solution of the one-bubble steady motion problem in terms of solid spherical harmonics (A1) is possible only for the near-to-spherical bubble shapes. The critical value of aspect ratio, empirically found by Meiron, is $\chi_c = 1.4$. Using the expansion (A6), it is rather straightforward to prove that the spherical-harmonics-based multipole expansion solution of the potential flow problem for a medium with a single spheroidal bubble is convergent if its aspect ratio $\chi < \sqrt{2} = 1.414\ldots$ and diverges otherwise. Substitution of (A6) into (3.1) gives us a formal series solution in terms of (A1), which is convergent at all the points $\boldsymbol{x}$ on the bubble surface if the condition $\|\boldsymbol{x}\| > d$ is satisfied uniformly. The minimum $\|\boldsymbol{x}\|$ value is achieved at the poles of an oblate spheroid, where $\boldsymbol{x} = \pm d\bar{\xi}_0 \boldsymbol{e}_1$. Thus, $\bar{\xi}_0 > 1$ and, hence, $\chi = \xi_0/\bar{\xi}_0/ < \sqrt{2}$ confirming the Meiron's finding.

Note that even for $\chi < \sqrt{2}$ the above solution contains an infinite series of harmonics and its convergence rate is rather slow, excluding only the small *We* case of essentially spherical bubbles. At the same time, a one-term solid-spheroidal-harmonics-based exact solution (3.1) exists for any χ.

REFERENCES

Aris, R. 1962 *Vectors, Tensors and the Basic Operations of Fluid Mechanics*. Prentice-Hall.

Batchelor, G. K. 1967 *An Introduction to Fluid Dynamics*. Cambridge University Press.

Bateman, G. & Erdelyi, A. 1953 *Higher Transcendental Functions*. McGraw Hill.

Biesheuvel, A. & van Wijngaarden, L. 1982 The motion of pairs of gas bubbles in a perfect fluid. *J. Engng Maths* **4**, 349.

Chesters, A. K. & Hoffman, G. 1982 Bubble coalescence in pure liquids. *Appl. Sci. Res.* **38**, 353.

Doubliez, L. 1991 The drainage and rupture of a non-foaming liquid film formed upon bubble impact with a free surface. *Intl J. Multiphase Flow* **17**, 783.

Duineveld, P. C. 1994 Bouncing and coalescence of two bubbles in water. PhD thesis, University of Twente.

Duineveld, P. C. 1995 The rise velocity and shape of bubbles in pure water at high Reynolds number. *J. Fluid Mech.* **292**, 325.

Gopinath, A. & Koch, D. L. 2002 Collision and rebound of small droplets in an incompressible, continuum gas. *J. Fluid Mech.* **454**, 145.

Hobson, E. W. 1931 *The Theory of Spherical and Ellipsoidal Harmonics*. Cambridge University Press.

Kang, I. S. & Leal, L. G. 1988 The drag coefficient for a spherical bubble in a uniform streaming flow. *Phys. Fluids* **31**, 233.

Kang, S. A., Sangani, A. S., Tsao, H.-K. & Koch, D. L. 1997 Rheology of dense bubble suspensions. *Phys. Fluids* **9**, 1540.

Kumaran, V. & Koch, D. L. 1994 The effect of hydrodynamic interactions on the averaged properties of a bidisperse suspension of high Reynolds number, low Reynolds number bubbles. *Phys. Fluids* A **5**, 1135.

Kushch, V. I. 1998 Elastic equilibrium of a medium containing a finite number of arbitrarily oriented spheroidal inclusions. *Intl J. Solids Structures* **35**, 1187.

Lessard, R. R. & Zieminski, S. A. 1971 Bubble coalescence and gas transfer in electrolytic aqueous solutions. *Ind. Engng Chem. Fundam.* **10**, 260.

Levich, V. 1962 *Physico-chemical Hydrodynamics*. Prentice Hall.

Magnaudet, J. & Eames, I. 2000 The motion of high-Reynolds number bubbles in inhomogeneous flows. *Annu. Rev. Fluid Mech.* **32**, 659.

Meiron, D. I. 1989 On the stability of gas bubbles rising in an inviscid fluid. *J. Fluid Mech.* **198**, 101.

Miksis, M., Vanden-Broeck, J.-M. & Keller, J. B. 1981 Axisymmetric bubble or drop in a uniform flow. *J. Fluid Mech.* **108**, 89.

Miksis, M., Vanden-Broeck, J.-M. & Keller, J. B. 1982 Rising bubbles. *J. Fluid Mech.* **123**, 31.

Moore, D. W. 1963 The boundary layer on a spherical gas bubbles. *J. Fluid Mech.* **16**, 161.

Moore, D. W. 1965 The velocity rise of distorted gas bubbles in a liquid of small viscosity. *J. Fluid Mech.* **23**, 749.

Pashley, R. M. 1981 Hydration forces between mica surfaces in aqueous electrolyte solutions. *J. Colloid. Interface Sci.* **80**, 153.

Ryskin, G. & Leal, L. G. 1984 Numerical solution of free-boundary problems in fluid mechanics. Part 2. Buoyancy-driven motion of a gas bubble through a quiescent liquid. *J. Fluid Mech.* **148**, 19.

Sangani, A. S. 1991 A pairwise interaction theory for determining the linear acoustic properties of dilute bubbly liquids. *J. Fluid Mech.* **232**, 221.

Sangani, A. S. & Didwania, A. K. 1993*a* Disperse phase stress tensor in flows of bubbly liquids at large Reynolds numbers. *J. Fluid Mech.* **248**, 27.

Sangani, A. S. & Didwania, A. K. 1993*b* Dynamics simulations of flows of bubbly liquids at large Reynolds numbers. *J. Fluid Mech.* **250**, 307.

Sangani, A. S. & Mo, G. 1996 An O(N) algorithm for Stokes and Laplace interactions of particles. *Phys. Fluids* **8**, 1990.

Sangani, A. S., Zhang, D. Z. & Prosperetti, A. 1991 The added mass, Basset, and viscous drag coefficients in nondilute bubbly liquids undergoing small-amplitude oscillatory motion. *Phys. Fluids* A **3**, 2955.

Smereka, P. 1993 On the motion of bubbles in a periodic box. *J. Fluid Mech.* **254**, 79.

Smereka, P. & Milton, G. W. 1991 Bubbly flow and its relation to conduction in composites. *J. Fluid Mech.* **233**, 65.

Spelt, P. D. M., Norato, M. A., Sangani, A. S., Greenwood, M. S. & Tavlarides, L. T. 2001 Attenuation of sound in concentrated suspensions: theory and experiments. *J. Fluid Mech.* **430**, 51.

Spelt, P. D. M. & Sangani, A. S. 1998 Properties and averaged equations for flows of bubbly liquids. *Appl. Sci. Res.* **58**, 337.

Tsao, H.-K. & Koch, D. L. 1994 Collisions of slightly deformable, high Reynolds number bubbles with short range repulsive forces. *Phys. Fluids* **6**, 2591.

Tsao, H.-K. & Koch, D. L. 1997 Observations of high Reynolds number bubbles interacting with a rigid wall. *Phys. Fluids* **9**, 44.

de Vries, A. W. G. 2001 Path and wake of a rising bubble. PhD thesis, University of Twente, The Netherlands.

VAN WIJNGAARDEN, L. 1993 The mean rise velocity of pairwise- interacting bubbles in liquid. *J. Fluid Mech.* **251**, 55.

VAN WIJNGAARDEN, L. & KAPTEYN, C. 1990 Concentration waves in dilute bubble/ liquid mixtures. *J. Fluid Mech.* **212**, 111.

YURKOVETSKY, Y. & BRADY, J. F. 1996 Statistical mechanics of bubbly liquid. *Phys. Fluids* **8**, 881.

ZENIT R., KOCH, D. L. & SANGANI, A. S. 2001 Measurements of the average properties of a suspension of bubbles rising in a vertical channel. *J. Fluid Mech.* **429**, 307.

ZUBER, N. 1964 On the dispersed two-phase flow in the laminar flow regime. *Chem. Engng Sci.* **19**, 897.